Fluid Flow, Dissolution, and Mixing Phenomena in Argon-Stirred Steel Ladles

HAOJIAN DUAN, LIFENG ZHANG, BRIAN G. THOMAS, and ALBERTO N. CONEJO[1]

In the current study, the multiphase fluid flow in argon-stirred steel ladles is simulated using an Eulerian–Lagrangian two-phase approach. The momentum source and the turbulent kinetic energy source due to the motion of the bubble are considered for the liquid phase. Argon bubbles are treated as discrete phase particles, and the interfacial forces between the bubbles and the liquid phase; the dependence of the gas density and the bubble diameter on the temperature and the static pressure; and the bubble size distribution are considered. When the fluid flow reaches the quasi-steady state, the ferroalloy melting and mixing phenomena is also modeled. The melting time and the trajectory length of each ferroalloy particle are recorded using a user-defined function (UDF). Local mixing time is predicted in the entire computational domain by checking the mixing criteria in every cell. The effects of gas flow rate, porous plug location, and separation angle of two porous plugs on the fluid flow and the mixing phenomena are investigated. The results show that the flow intensity increases, and the mixing time decreases with the increasing gas flow rate. The optimal porous plug's radial position with one porous plug is 0.50*R* for its best mixing condition. When two porous plugs are adopted, the separation angle of 90 deg is recommended to improve the flow field and mixing phenomena.

https://doi.org/10.1007/s11663-018-1350-4

I. INTRODUCTION

GAS injection into steel ladles is a commonly used technology in the secondary refining process to promote the stirring of liquid steel, to homogenize the temperature and chemical composition, to remove inclusions, and to enhance the slag–metal reactions. Bubbles are successively formed from porous plugs located at the base of the ladle. Due to buoyancy, the bubbles rise up and generate a recirculation flow pattern in the ladle, which is significant for the melting and dissolution of the ferroalloys added into the ladle; for the diffusion and convection of the mass and heat; for the coagulation, agglomeration, and floatation of inclusions; and for the emulsification of the top slag phase, *etc*. However, improper operations can cause a large number of problems, such as reoxidation, entrainment of the slag phase, and the enhancement of refractory wearing. Therefore, it is imperative that a proper simulation of the gas-stirred process is needed to understand the various phenomena in the gas-stirred ladle system.[1]

During the past several decades, many physical models and computational models have been developed to investigate the fluid flow and mixing phenomena in gas-stirred ladles. Considerable efforts have been made by various groups of researchers to investigate underlying process dynamics in gas-stirred aqueous as well as low-melting-point alloy systems using physical modeling.[2–5] These studies provided the necessary information to understand the related phenomena, such as hydrodynamics and mixing, in gas-stirred ladles. However, physical models can never provide more than a reasonable estimate because of geometric scale factors and physical properties.

Computational modeling plays a very important role in understanding the hydrodynamics, turbulence, mixing phenomena, *etc*., due to a lack of optical accessibility and the high temperature in industrial ladles. Currently, there are mainly three different approaches[6] to describe the gas–liquid two-phase flow in gas-stirred ladles, namely: (1) the quasi-single-phase model[7–15]; (2) the Eulerian–Eulerian multiphase approach[16–23]; and (3) the Eulerian–Lagrangian multiphase approach.[24–28] Table I lists the summary of previous publications that have investigated the fluid flow in argon-stirred steel ladles.

The quasi-single phase model is the earliest attempt to model fluid flow in gas-stirred ladles, and it still retains

HAOJIAN DUAN, LIFENG ZHANG, and ALBERTO N. CONEJO are with the School of Metallurgical and Ecological Engineering, University of Science and Technology Beijing, Beijing 100083, P.R. China. Contact e-mail: zhanglifeng@ustb.edu.cn BRIAN G. THOMAS is with the Department of Mechanical Engineering, Colorado School of Mines, Golden, CO 80401 and also with the Department of Mechanical Science and Engineering, University of Illinois at Urbana-Champaign, Urbana, IL 61801.

Manuscript submitted February 5, 2018.
Article published online July 26, 2018.

Table I. Summary of Simulation Studies of Fluid Flow in Argon-Stirred Ladles

Year	Author	Methods	Main Work
1975	Szekely *et al.*[7]	Q-S	velocity and turbulence energy fields were predicted by solving the turbulent Navier–Stokes equations with Spalding's k-W model for the turbulence viscosity
1978	Roy *et al.*[56]	Q-S	flows in a gas-agitated cylindrical were predicted using quasi-single phase model the void fraction was estimated for two different situations: with the slip between gas and liquid phases and without any slip
1981	Roy and Majumdar[8]	Q-S	velocity fields and turbulence levels were calculate using quasi-single phase model the void fraction was estimated for slip condition in the two-phase region
1985	Salcudean *et al.*[57]	Q-S	mass, momentum, energy, and concentration equations were solved for the buoyancy driven transient flows the turbulence was simulated by using zero order and differential models of turbulence
1988	Johansen and Boysan[24]	E-L	momentum interaction terms, the void fraction, and the turbulence production due to bubbles were calculated the drag, pressure, added mass, and gravitational effects were considered the turbulent flow close to the free surface was considered
1988	Salcudean and Lai[58]	E-E	Navier–Stokes equations for the liquid phase were solved together with the simplified conservation equations for the gaseous phase the turbulence was simulated by the k-ε model
1989	Castillejos *et al.*[10]	Q-S	the transient fluid flow and temperature distributions in argon-stirred ladles have been investigated the two-phase zone was modeled by novel experimental equations
1990	Turkoglu *et al.*[59]	E-E	flow and temperature fields due to bottom air injection were predicted in a cylindrical vessel containing water the turbulence in the liquid phase was modeled using a two-equation k-ε model the interphase friction and heat transfer coefficients were calculated by using correlations available in the literature
1990	Woo *et al.*[11]	Q-S	the velocity field and the map of the turbulent kinetic energy were computed in a water model of an argon-stirred ladle the experimentally determined void fraction distribution was used in computing the body force driving the flow
1991	Turkoglu and Farouk[16]	E-E	flow and concentration fields were studied in bench scale gas-injected molten steel baths the dependency of flow structure and mixing characteristics on bath aspect ratio and gas-injection rate was numerically studied.
1992	Turkoglu and Farouk[60]	E-E	flow and temperature fields were analyzed in a bench-scale gas-injected molten steel bath the interphase momentum exchange and the interphase heat transfer were considered
1995	Sheng and Irons[27]	E-L	the liquid flow field was first calculated in an Eulerian frame with an estimated distribution of the void fraction trajectories of bubbles were then computed in a Lagrangian manner using the estimated flow field, experimentally measured information on bubble drag coefficients, lateral migration due to lateral lift forces, and variation in bubble size due to breakup the turbulence in the two-phase zone was modeled with a modified k-ε model with extra source terms to account for the second phase
1995	Zhu *et al.*[13]	Q-S	the flow pattern and mixing phenomena in argon-stirred ladles with different types of tuyere arrangement were investigated.
1996	Zhu *et al.*[14]	Q-S	effects of gas flow rate, positions of nozzle and tracer, and inclined wall on the flow pattern and mixing in argon-stirred ladles were investigated
1998	Ilegbusi *et al.*[61]	E-E	transport equations for the variables of each phase were solved, with allowance for interface transfer of momentum the turbulence was represented by a modified k-ε model, with allowance for turbulence modulation by the bubbles through enhancement of the source terms in the equations for k and ε
1999	Guo和 Irons[28]	E-L	the buoyancy, drag, lift, virtual mass, and pressure gradient force were considered the lateral lift force was responsible for plume spreading, whereas the lateral drag force caused plume bending.
2000	Zhang[17]	E-E	the interphase drag force, the turbulent model, the size of bubble and the gas-injection mode on the fluid flow were discussed
2001	Han *et al.*[62]	E-E	the fluid flow and the mixing behavior in a gas-stirred ladle with oil layer were investigated using water model experiments and numerical simulation
2003	Xia and Ahokainen[63]	E-E	the transient two-phase flow and the heat transfer in a gas-stirred steelmaking ladle were investigated the effect of heat transfer at the bubble–liquid steel interface on the flow and thermal fields was assessed

Table I. continued

Year	Author	Methods	Main Work
2004	Aoki and Thomas[41]	E-L	the buoyancy force and the drag force were considered
2005	Madan *et al.*[15]	Q-S	a quasi-single-phase model was developed to predict mixing times in ladles fitted with dual plugs
			two distinct possibilities were examined to estimate the gas volume fraction, namely, with no slippage between gas and liquid phases and without slip
2005	Mendez *et al.*[32]	E-E	effects of drag and non-drag forces (such as virtual mass, lift, and turbulent dispersion force) on the numerical results in metallurgical ladles were investigated
			other effects such as the turbulence increment, the bubble size, and the deformable free surface were also considered
2008	Li *et al.*[20]	E-E	multiphase volume of fluid (VOF) method was used to simulate the three-phase flows and behaviors of slag/steel interface in an argon gas-stirred ladle
2009	Olsen and Cloete[64]	E-E	the VOF model was used to track the liquid phase and top gas
		E-L	bubbles were modeled as discrete particles, and five forces were accounted for: buoyancy, drag, lift, virtual mass, and turbulent dispersion
2011	Liu *et al.*[34]	E-E	the VOF model was used to track any interface between two or more immiscible phases, which
		E-L	include slag/metal, slag/gas, and metal/gas
			gas bubbles were treated as discrete second phase, and the trajectory of each bubble was calculated in each time step according to the drag, the buoyancy, the virtual mass and pressure gradient force.
2013	Lou and Zhu[22]	E-E	interaction forces between gas–liquid two phases were considered, such as the drag force, the lift force, and the turbulent dispersion force due to liquid velocity fluctuation
			the modified k-ε model with extra source terms to account for the bubble-induced turbulence was adopted to model the turbulence in the system
2015	Li *et al.*[36]	E-E	the VOF model was used to track the free surfaces by solving a single set of momentum
		E-L	equations and tracking the volume fraction of each fluid
			gas bubbles were tracked using the DPM, and the buoyancy, drag force, virtual mass force, and pressure gradient force were included
			the LES turbulence model was taken to describe the turbulence in the system

Q-S, Quasi-single phase model; E-E, Eulerian–Eulerian multiphase approach; E-L, Eulerian–Lagrangian multiphase approach).

popularity today for its low computational cost. In this model, the gas–liquid mixture phase is assumed to be a homogeneous liquid of reduced density, and various plume parameters such as plume dimensions, the gas volume fraction distribution, and the bubble slip velocity are specified a priori in the numerical solution scheme. However, the adequacy of the quasi-single phase model has been an issue of debate because the gas–liquid plume zone is fixed in space and the interaction forces between the gas phase and the liquid phase, such as the drag force, the lift force, the virtual mass force *etc*., are neglected in the model.

In the Eulerian–Eulerian multiphase approach, both gas phase and liquid phase are treated mathematically as interpenetrating continua under an Eulerian frame of reference, and the continuity and the momentum conservation equations are solved separately for each phase. The concept of phase volume fraction is introduced, and the phases are assumed to share space in proportion to their volume fractions. These volume fractions are satisfied with continuous functions of space and time and the sum of volume fractions is equal to unit. Interaction forces between the gas phase and the liquid phase are considered as momentum exchange source terms in the momentum equations, which have to be modified to take into account the phase volume fraction. During the bubble-rising process, the additional liquid turbulent kinetic energy is produced by the motion of bubbles. The additional turbulent kinetic energy is generally accounted for by source terms in the turbulence model.[29,30] To account for the turbulent dispersion of bubbles, some researchers[22,31,32] proposed the concepts of turbulent diffusion force to describe the diffusion of the bubbles due to turbulence, which was modeled as a force term in the momentum conservation equation. However, it is difficult to consider the spectrum of bubble size and predict the real motion of the gas phase as discrete bubbles using the Eulerian–Eulerian approach.[6,33]

In the Eulerian–Lagrangian multiphase approach, the continuity and the momentum conservation equations are solved only for the liquid phase in a fixed or Eulerian frame of reference, while the dispersed bubbles moving through the fluid are tracked explicitly by solving their Newtonian equations of motion under a Lagrangian frame of reference. The trajectory equations of bubbles have to consider the balance of all relevant forces acting on the gas bubbles. Additionally, in order to incorporate the momentum transfer from the bubbles to the liquid, a momentum source term has to be introduced into the Navier–Stokes equation for the liquid phase. The clear advantages of the Eulerian–Lagrangian approach are the simplicity of formulation, the detailed description of bubble dynamics, easy incorporation of bubble size distribution spectrum, the ability to account for direct bubble–bubble interactions and the computational efficiency. Johansen and Boysan[24] were among the first to model bubble-stirred ladles using the Eulerian–Lagrangian approach. They adopted the shear work performed on the liquid by a single bubble equaling to the product of the drag force and the relative velocity to

represent the additional turbulence production and paid special attention to the flow close to the free surface and in the bubble plume. The model predictions showed satisfactory quantitative agreement with experimental results for mean velocities and turbulence quantities. Based on the experimental findings, Sheng and Irons[27] calculated the liquid flow field in an Eulerian frame with an estimated distribution of the void fraction and then computed the trajectories of bubbles in a Lagrangian manner using the estimated flow field. Four phenomena associated with bubble dynamics were discussed: the variation of the bubble at different heights, the slip velocity between the bubbles and the liquid, the lateral motion of the bubbles, and the effects of bubbles on turbulence in the plume. Guo and Irons[28] developed a three-dimensional, Eulerian–Lagrangian model to investigate the gas–liquid flow in a ladle and found that the lateral lift force is responsible for plume spreading, whereas the lateral drag force bend the plume. It should be noted that the bubble size distribution was ignored and the bubble density and bubble size remained constant during flotation in the previous studies.

In recent years, several researchers have employed the combined multiphase model to investigate the bubble flow and slag layer behavior in gas-stirred ladles.[34–36] The bubbles are tracked as discrete particles using the Lagrangian discrete phase model (DPM), whereas the interfaces between metal, slag and gas are tracked using the Eulerian volume of fluid (VOF) model. However, some interaction forces between the gas phase and the liquid phase, such as the lift force, have not been considered, and the effect of bubble-induced turbulence is also neglected in these models.

There have been many publications[5,12–16,21,23,35,37–40] that address the modeling of mixing phenomena in gas-stirred ladles, but few of them[41] have considered the melting process of the addition. With the current understanding of mixing phenomena in bottom-stirred metallurgical ladles, it is now possible to extend the models to describe their melting and dissolution behaviors. Taniguch *et al.*[42] developed a hot model to study the effect of gas injection on the melting rate of a solid sphere in a liquid bath. Tanaka *et al.*[42] have used Newton's second law of motion to describe the subsurface trajectories of spherical particles during simulated furnace to ladle tapping operations in steelmaking. Zhang and Oeters[43] developed a mathematical model for the melting of ferromanganese particles in liquid iron in a ladle and found that the melting behavior is greatly affected by the particle size distribution, the melt temperature, and the particle-melt slip velocity.

In the current study, the melting and mixing phenomena of a ferroalloy during bottom gas stirring in a ladle was investigated *via* a three-dimensional transient model based on the Eulerian–Lagrangian multiphase approach. First, the multiphase flow model includes interfacial forces between bubbles and the liquid phase, the density, and diameter of argon bubbles as well as the bubble size distribution. Second, the melting of the ferroalloy and the mixing map in the ladle are determined. Lastly, variables considered on the fluid flow and mixing phenomena are the gas flow rate, porous plug location, and its separation angle.

II. MATHEMATICAL MODEL

A. *Fluid Flow*

The dynamic simulation of the multiphase flow evolving in gas-stirred ladles is carried out using a combined Eulerian–Lagrangian multiphase approach. The liquid phase flow is calculated by solving the unsteady Reynolds-averaged Navier–Stokes (RANS) conservation equations containing liquid volume fraction α_l. In order to close the equations, the well-known standard k-ε two-equation turbulence model is adopted, extended by accounting for the effects of gas bubbles.

The continuity equation and momentum conservation equations for the liquid phase are as follows:

$$\frac{\partial}{\partial t}(\alpha_l \cdot \rho_l) + \nabla \cdot (\alpha_l \cdot \rho_l \cdot \vec{u_l}) = 0 \quad [1]$$

$$\frac{\partial}{\partial t}(\alpha_l \cdot \rho_l \cdot \vec{u_l}) + \vec{u_l} \cdot \nabla(\alpha_l \cdot \rho_l \cdot \vec{u_l}) - \nabla \cdot [\alpha_l(\mu_l + \mu_t)]\nabla \vec{u_l} = -\nabla P - \vec{F_b} \quad [2]$$

where α_l is the liquid volume fraction; ρ_l is the density of liquid steel (kg/m^3); $\vec{u_l}$ is the time-averaged fluid velocity (m/s); P is the pressure (Pa); μ_l is the molecular viscosity of liquid steel (Pa·s); and μ_t is the turbulent viscosity (Pa·s), as described later.

F_b is the momentum source from the bubble motion, which can be evaluated readily from the concept that the interfacial forces experienced by the bubbles act with equal magnitude but in opposite directions in the liquid phase.

$$\vec{F_b} = \frac{\alpha_l}{\Delta V_{cell}} \sum_{i}^{N_{b,cell}} \left(\overrightarrow{F_{D,i}} + \vec{F_{VM,i}} + \vec{F_{L,i}} + \vec{F_{P,i}} \right) Q^s_{b,i} \Delta t \quad [3]$$

where V_{cell} is the computational cell volume (m^3); $N_{b,cell}$ is the total number of bubbles in the computational cell volume; $Q^s_{b,i}$ is the flow rate of the injected bubble stream (kg/s); t is the time step of bubble trajectory calculation (s); and$F_{D,i}$, $F_{VM,i}$, $F_{L,i}$ and $F_{P,i}$ are the drag force, the virtual mass force, the lift force, and the pressure gradient force, as described later.

The standard k-ε two-equation turbulence model as proposed by Launder and Spalding is adopted for the fluid turbulence. The turbulence kinetic energy, k, and its rate of dissipation, ε, are obtained from the following transport equations:

$$\alpha_l \rho_l \left(\frac{\partial k}{\partial t} + \vec{u_l} \cdot \nabla k \right) = \nabla \cdot \left(\alpha_l \frac{\mu_t}{\sigma_k} \nabla k \right) + \alpha_l G_k - \alpha_l \rho_l \varepsilon + \alpha_l (S_{k,b} + S_{k,surf}) \quad [4]$$

$$\alpha_l \rho_l \left(\frac{\partial \varepsilon}{\partial t} + \vec{u_l} \cdot \nabla \varepsilon \right) = \nabla \cdot \left(\alpha_l \frac{\mu_t}{\sigma_\varepsilon} \nabla \varepsilon \right) + \alpha_l C_1 \frac{\varepsilon}{k} (G_k + S_{k,b} + S_{k,surf}) - \alpha_l C_2 \rho_l \frac{\varepsilon^2}{k} \quad [5]$$

The turbulent viscosity, μ_t, is computed by combining k and ε as follows:

$$\mu_t = \rho_l C_\mu \frac{k^2}{\varepsilon} \quad [6]$$

where C_1, C_2, C_μ, σ_k, and σ_ε are the empirical constants, values of which are 1.44, 1.92, 0.09, 1.0, and 1.3 respectively; and G_k is the generation of turbulent kinetic energy, obtained as follows:

$$G_k = -\mu_t \left(\frac{\partial u_{l,i}}{\partial x_j} + \frac{\partial u_{l,j}}{\partial x_i} \right) \frac{\partial u_{l,j}}{\partial x_i} \quad [7]$$

It is now generally accepted that the bubbles contribute significantly to the production of turbulence in the argon-stirred ladle. The source term of turbulent kinetic energy due to bubbles can be considered to be equivalent to the shear work performed on the liquid phase by the bubbles. According to the study of Johansen and Boysan,[24] the shear work performed on the liquid phase by a single bubble is equal to the product of the drag force and the relative velocity. Therefore, the source term of turbulent kinetic energy per unit volume, $S_{k,b}$, can be calculated from the following expression:

$$S_{k,b} = \frac{C_{sk}}{\Delta V_{cell}} \sum_i^{N_{b,cell}} \vec{F_b} \cdot (\vec{u_l} - \vec{u_{b,i}}) Q^s_{b,i} \Delta t \quad [8]$$

where $\vec{u_{b,i}}$ is the time-averaged velocity of ith bubble (m/s); C_{sk} is a constant to be empirically determined, and the value of C_{sk} is set to 0.12 based on the calculated results obtained by Aoki *et al.*[41]

The effect of the free surface where turbulence is damped due to local surface shape deformation is taken into account by the same procedure as Johansen and Boysan.[24] Near the free surface, the turbulent kinetic energy is modified as follows:

$$S_{k,surf} = \mu_t \frac{C'_1}{C'_1 + 1.5C'_3} \frac{C'_1}{C'_1 + 2C'_3} \left(\frac{\partial u_1}{\partial x_2} + \frac{\partial u_2}{\partial x_1} \right) \frac{\partial u_{l,j}}{\partial x_i}, \quad [9]$$

where u_1 and u_2 are the mean velocity components parallel and normal to the free surface (m/s); x_1 and x_2 are the coordinates of parallel and normal directions (m). $C'_1 = 2.5$ is a constant and $C'_3$is a coefficient which takes a value of 1.0 at the free surface and is damped along the normal direction as

$$C'_3 = \exp\left(\frac{\Delta y}{l_s} \right), \quad [10]$$

where Δy is the distance from the free surface (m) and l_s is the eddy length scale calculated as follows:

$$l_s = \frac{C_\mu^{3/4} k^{3/2}}{\kappa \varepsilon} \quad [11]$$

where $\kappa = 0.4$ is the von Karman constant.

Bubble and liquid volume fractions are calculated by statistics of the number and the residence time of discrete bubbles in a given control cell as follow[24]:

$$\alpha_b = \frac{1}{\Delta V_{cell}} \sum_i^{N_{b,cell}} \frac{Q^s_{b,i} \Delta t}{\rho_{b,i}} \quad [12]$$

$$\alpha_l = 1 - \alpha_b \quad [13]$$

where $\rho_{b,i}$ is the density of ith bubble (kg/m^3).

The simulation of the gas bubbles, as mentioned already, has been carried out by the Lagrangian approach, in which the gas bubble is treated as a discrete phase and the motion of the individual bubble is solved by integrating the balance of the gravity and buoyancy force, the drag force, the virtual mass force, the lift force and the pressure gradient force. Argon bubbles are assumed to be spherical, and bubble–bubble collisions are assumed to be negligible. The Lagrangian form of Newton's second law of motion can be conveniently represented, and it can be described as:

$$\frac{d\vec{u_{b,i}}}{dt} = \vec{F}_{G,i} + \vec{F}_{B,i} + \vec{F}_{D,i} + \vec{F}_{VM,i} + \vec{F}_{L,i} + \vec{F}_{P,i} \quad [14]$$

The terms on the right-hand side represent the gravity and buoyancy force, the drag force, the virtual mass force, the lift force, and the pressure gradient force, respectively. Integration of time yields the velocity of the

Table II. Property Parameters of Employed in the Current Study

Property	Symbol	Value	Unit
Density of molten steel	ρ_l	7020	kg/m^3
Viscosity of molten steel	μ_l	0.0067	Pa s
Heat capacity of liquid steel	$C_{p,M}$	820	J/kg K
Thermal conductivity of liquid steel	k_M	40.3	J/m s K
Diffusion coefficient of the solute	D_M	5.5×10^{-5}	m^2/s
Surface tension of liquid/bubble	σ_{lb}	1.4	N/m
Density of argon gas (STP)	ρ_{0b}	1.784	kg/m^3
Density of ferroalloy	ρ_A	6120	kg/m^3
Heat capacity of ferroalloy	$C_{p,A}$	845.7	J/kg K

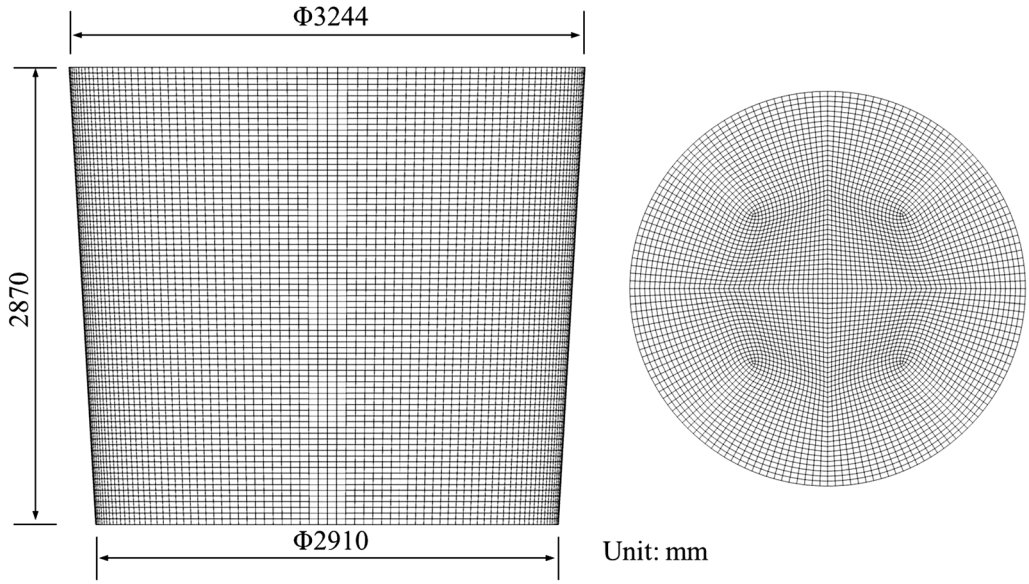

Fig. 1—Geometry and mesh of computational domain.

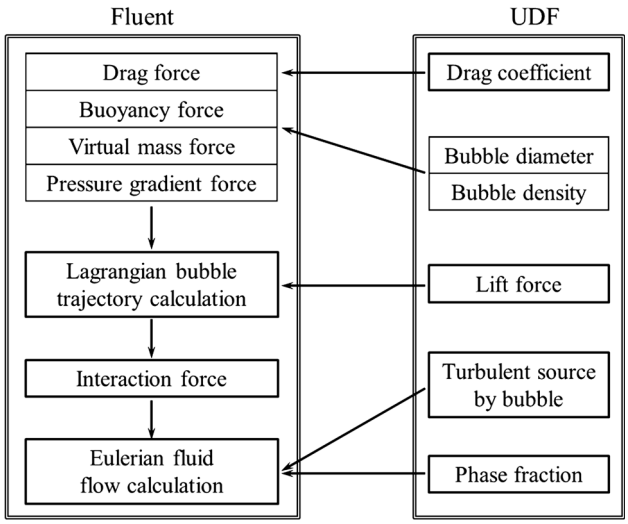

Fig. 2—Flow chart of fluid flow model.

bubble at each point along the trajectory, with the trajectory itself predicted by

$$\vec{x}_{\mathrm{b},i} = \int \vec{u}_{\mathrm{b},i}\, dt \qquad [15]$$

The chaotic effect of turbulence on the bubble trajectory is incorporated with the "random walk" method. The instantaneous liquid velocity $\vec{u}_{\mathrm{l}}$ in Eq. [14] is the sum of the time-averaged velocity and the fluctuation component; the latter varies in proportion to the local turbulence level using a random number with normal Gaussian distribution:

$$\vec{u}_{\mathrm{l}} = \overline{\vec{u}}_{\mathrm{l}} + \vec{u}_{\mathrm{l}}' = \overline{\vec{u}}_{\mathrm{l}} + \varsigma\sqrt{\frac{2k}{3}}\vec{e}_{\mathrm{R}} \qquad [16]$$

where $\overline{\vec{u}}_{\mathrm{l}}$ is the mean flow velocity (m/s); $\vec{u}_{\mathrm{l}}'$ is the fluctuation velocity (m/s); k is the turbulent kinetic energy ($\mathrm{m}^2/\mathrm{s}^2$); and $\vec{e}_{\mathrm{R}}$ is a randomly oriented unit vector.

The motion of gas bubbles in the liquid is mainly driven by the buoyancy, and the combined effect of the gravity and buoyancy forces on the gas bubbles is expressed as follows:

$$\vec{F}_{\mathrm{G},i} + \vec{F}_{\mathrm{B},i} = \frac{\rho_{\mathrm{b},i} - \rho_{\mathrm{l}}}{\rho_{\mathrm{b},i}}\vec{g} \qquad [17]$$

The drag force acts opposite to the relative motion of bubble moving through the liquid flow field, which consists of a form drag and a friction drag exerted by the liquid on the moving bubble and represents the predominant resistance to the upward movement of the gas bubble in the liquid bath.

The drag force depends on the Reynolds number of gas bubbles, the viscosity of the liquid, the size of bubble, the density of bubble, and the relative velocity between the liquid and the gas by the following equation.

$$\vec{F}_{\mathrm{D},i} = \frac{18\mu_{\mathrm{l}}C_{\mathrm{D},i}\mathrm{Re}_i}{24d_{\mathrm{b},i}^2\rho_{\mathrm{b},i}}\left(\vec{u}_{\mathrm{l}} - \vec{u}_{\mathrm{b},i}\right) \qquad [18]$$

where $d_{\mathrm{b},i}$ is the diameter of ith bubble (m); Re_i is the particle Reynolds number which is defined in terms of the relative velocity between the fluid and the bubble as follows:

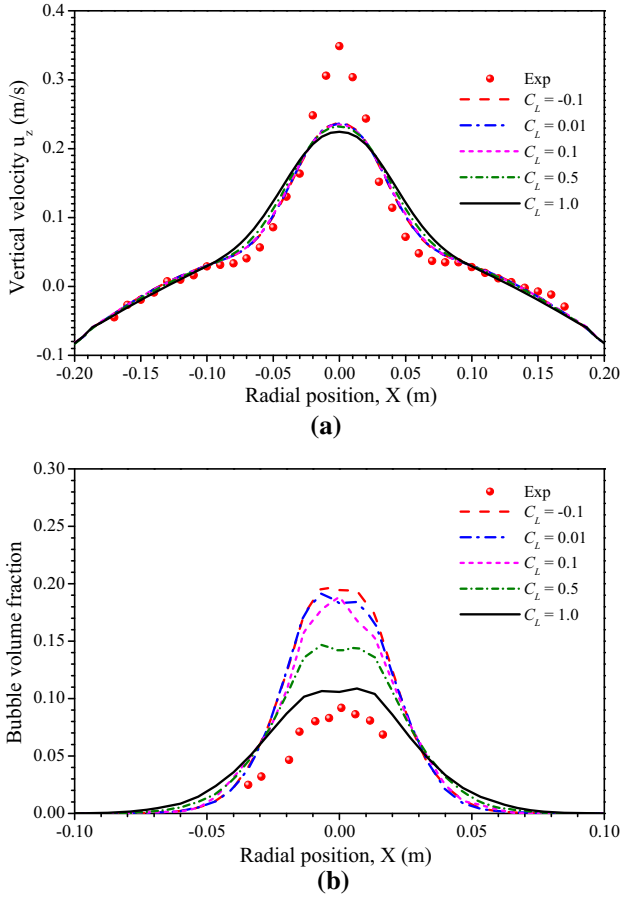

Fig. 3—Comparison of (*a*) vertical liquid velocity and (*b*) bubble volume fraction between simulation and experiment.

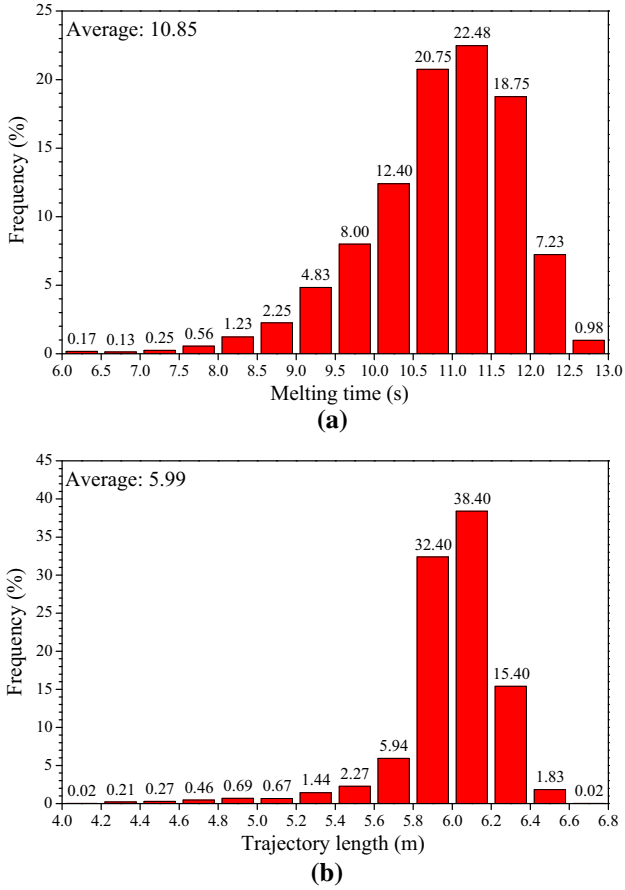

Fig. 5—(*a*) Melting time distribution and (*b*) trajectory length distribution during the melting process in the case of the superheat of 60 K and the ferroalloy diameter of 30 mm.

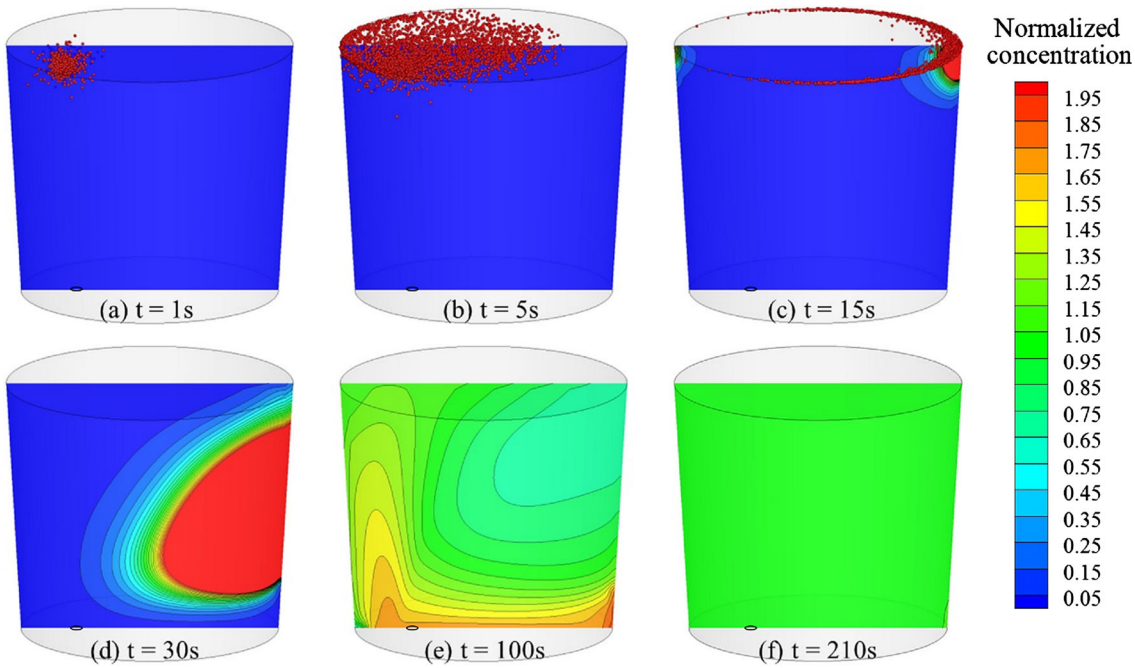

Fig. 4—Concentration profiles during the dissolution process of FeMn as a function of time using one porous plug located at 0.68*R* and a gas flow rate of 220 NL/min. (*a*) *t* = 1 s, (*b*) *t* = 5 s, (*c*) *t* = 15 s, (*d*) *t* = 30 s, (*e*) *t* = 100 s, (*f*) t = 210 s.

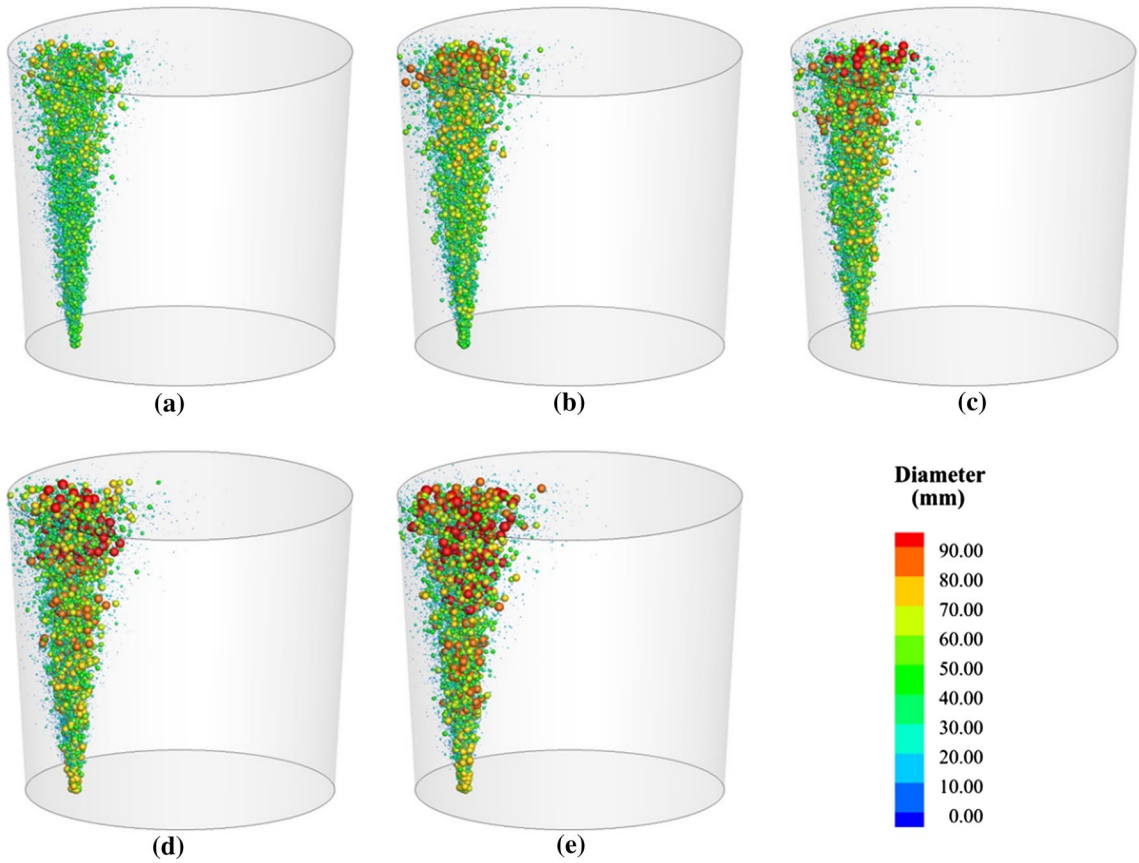

Fig. 6—Predicted bubble distribution in 150-ton gas-stirred ladle at different gas flow rates. (*a*) 120 NL/min, (*b*) 170 NL/min, (*c*) 220 NL/min, (*d*) 270 NL/min, (*e*) 320 NL/min.

$$\mathrm{Re}_i = \frac{\rho_\mathrm{l} d_{\mathrm{b},i} \left(\vec{u_\mathrm{l}} - \vec{u_{\mathrm{b},i}} \right)}{\mu_\mathrm{l}} \qquad [19]$$

The drag coefficient $C_{\mathrm{D},i}$ is from Kuo and Wallis,[44] which takes the bubble shape change into account according to its diameter.

$$\begin{aligned}
C_{\mathrm{D},i} &= \frac{16}{\mathrm{Re}_i} \quad \mathrm{Re}_i \le 0.49 \\
C_{\mathrm{D},i} &= \frac{20.68}{\mathrm{Re}_i^{0.643}} \quad 0.49 < \mathrm{Re}_i \le 100 \\
C_{\mathrm{D},i} &= \frac{6.3}{\mathrm{Re}_i^{0.385}} \quad \mathrm{Re}_i > 100, \mathrm{We} \le 8, \mathrm{Re}_i \le \frac{2065.1}{\mathrm{We}^{2.6}} \\
C_{\mathrm{D},i} &= \frac{\mathrm{We}}{3} \quad \mathrm{Re}_i > 100, \mathrm{We} \le 8, \mathrm{Re}_i > \frac{2065.1}{\mathrm{We}^{2.6}} \\
C_{\mathrm{D},i} &= \frac{8}{3} \quad \mathrm{Re}_i > 100, \mathrm{We} > 8
\end{aligned} \qquad [20]$$

We is the Weber number defined as follows.

$$\mathrm{We} = \frac{\rho_\mathrm{l} d_{\mathrm{b},i} \left| \vec{u_\mathrm{l}} - \vec{u_{\mathrm{b},i}} \right|^2}{\sigma_{\mathrm{lb}}} \qquad [21]$$

where σ_{lb} is the surface tension between the liquid and the bubble (N/m).

If bubbles are accelerated relative to the liquid, then part of the surrounding liquid has to be accelerated as well. The resistance to the acceleration is due to a "virtual mass" of liquid that has to be accelerated when a bubble accelerates and the additional force is called as the virtual mass force. The virtual mass coefficient C_{VM} is equal to 0.5, which is the theoretical value of a spherical particle moving in the fluid.

$$\vec{F_{\mathrm{VM},i}} = C_{\mathrm{VM}} \frac{\rho_\mathrm{l}}{\rho_{\mathrm{b},i}} \frac{\mathrm{d}}{\mathrm{d}t} \left(\vec{u_\mathrm{l}} - \vec{u_{\mathrm{b},i}} \right) \qquad [22]$$

When the bubble rises in the liquid, there exists an unsymmetrical pressure distribution on its external boundary. Pressure is the lowest in the region of the largest relative velocity, and therefore, the bubble is driven into this region due to a lift force. The lift force mainly includes the Magnus force resulting from the unsymmetrical pressure distribution and the Saffman force due to the shear in the mean flow. The lift force depends on the vector product of the slip velocity and the curl of the liquid velocity, and therefore, the lift force acts in a direction perpendicular to both the slip velocity and the curl of the liquid velocity field. For the lift

coefficient C_L, Pourtousi *et al.*[45] suggested that the lift coefficient C_L for bubbly flow regime with small spherical bubbles was in the range of 0.1 to 0.5. Bertodano *et al.*[46] suggested the value between 0.02 and 0.1 in bubbly flows in vertical ducts. Sheng and Irons[27] measured the value of the lift coefficient C_L to be 0.1 in plumes with small bubbles. Zhang[17] and Guo and Irons[28] clearly described a better agreement with experimental data when the lift force was considered correct.

$$\vec{F}_{L,i} = C_L \frac{\rho_l}{\rho_{b,i}} \left(\vec{u_l} - \vec{u_{b,i}} \right) \times \nabla \times \vec{u_l} \qquad [23]$$

The pressure gradient force arises due to the difference in pressure across the bubble surface and always directs from the region of higher-pressure to the region of lower-pressure.

$$\vec{F}_{P,i} = \frac{\rho_l}{\rho_{b,i}} \vec{u_l} \cdot \nabla \vec{u_l} \qquad [24]$$

The effects of temperature and static pressure on the gas density and the bubble diameter are usually neglected for simulating fluid flow in previous studies. In the liquid steel, however, the volume expansion of a bubble along the vertical direction due to the static pressure and the temperature change is not negligible. Thus, accurate calculations of the gas density and the bubble diameter are important in the simulation. The density and the diameter of bubbles in the computational domain are calculated by the ideal gas law, according to the local static pressure at each position and the temperature:

$$\rho_{b,i} = \rho_{0b} \frac{p_0 + \rho_l g(H - y_i)}{p_0} \frac{T_0}{T} \qquad [25]$$

$$\rho_b^{\text{bottom}} = \rho_{0b} \frac{p_0 + \rho_l g H}{p_0} \frac{T_0}{T} \qquad [26]$$

$$d_{b,i} = \sqrt[3]{\frac{\rho_b^{\text{bottom}}}{\rho_{b,i}}} d_b^{\text{bottom}} = \sqrt[3]{\frac{p_0 + \rho_l g H}{p_0 + \rho_l g(H - y_i)}} d_b^{\text{bottom}} \qquad [27]$$

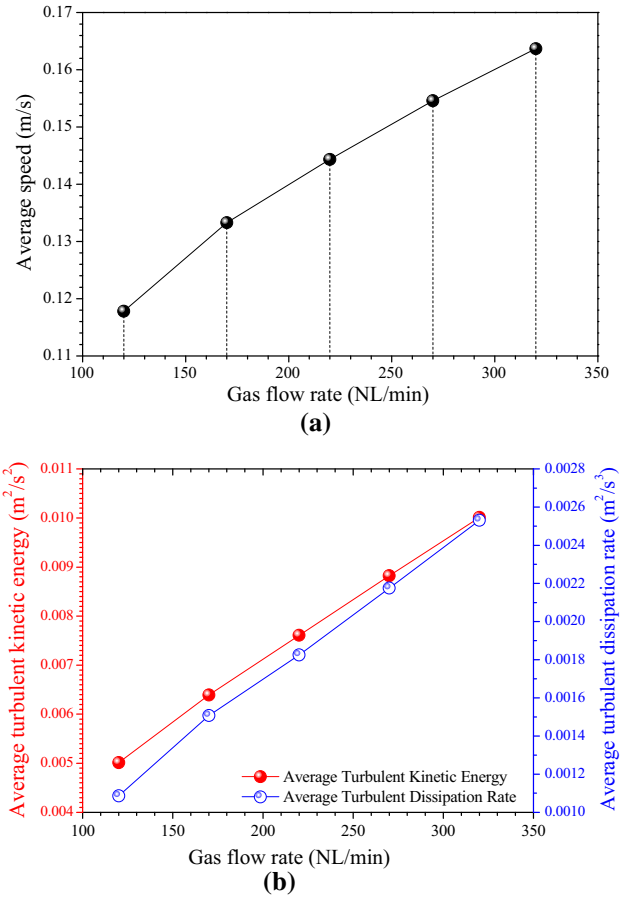

Fig. 7—Effect of gas flow rate on (*a*) average speed, (*b*) average turbulent kinetic energy and its dissipation rate.

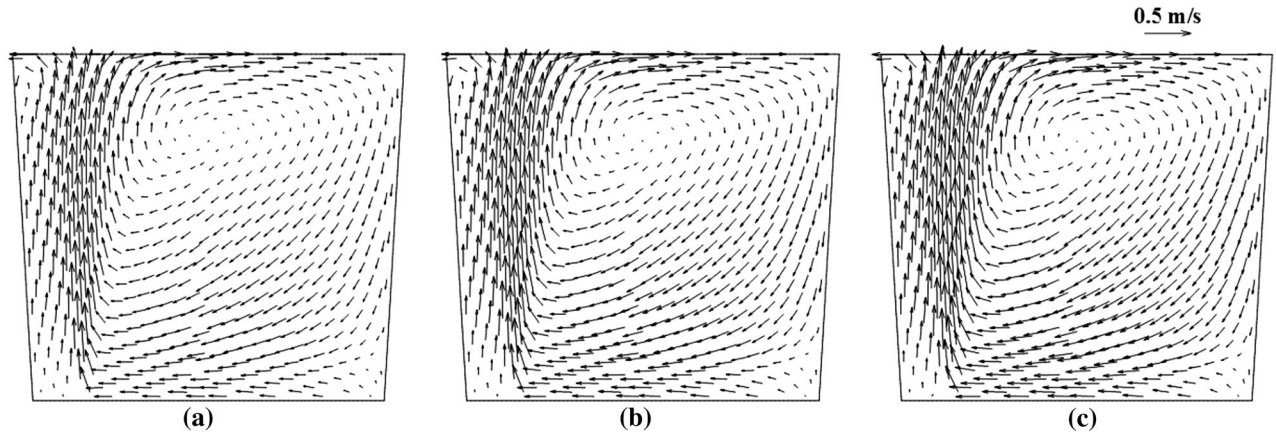

Fig. 8—Predicted velocity field in the vertical plane of 150-ton gas-stirred ladle at different gas flow rates. (*a*) 120 NL/min, (*b*) 220 NL/min, (*c*) 320 NL/min.

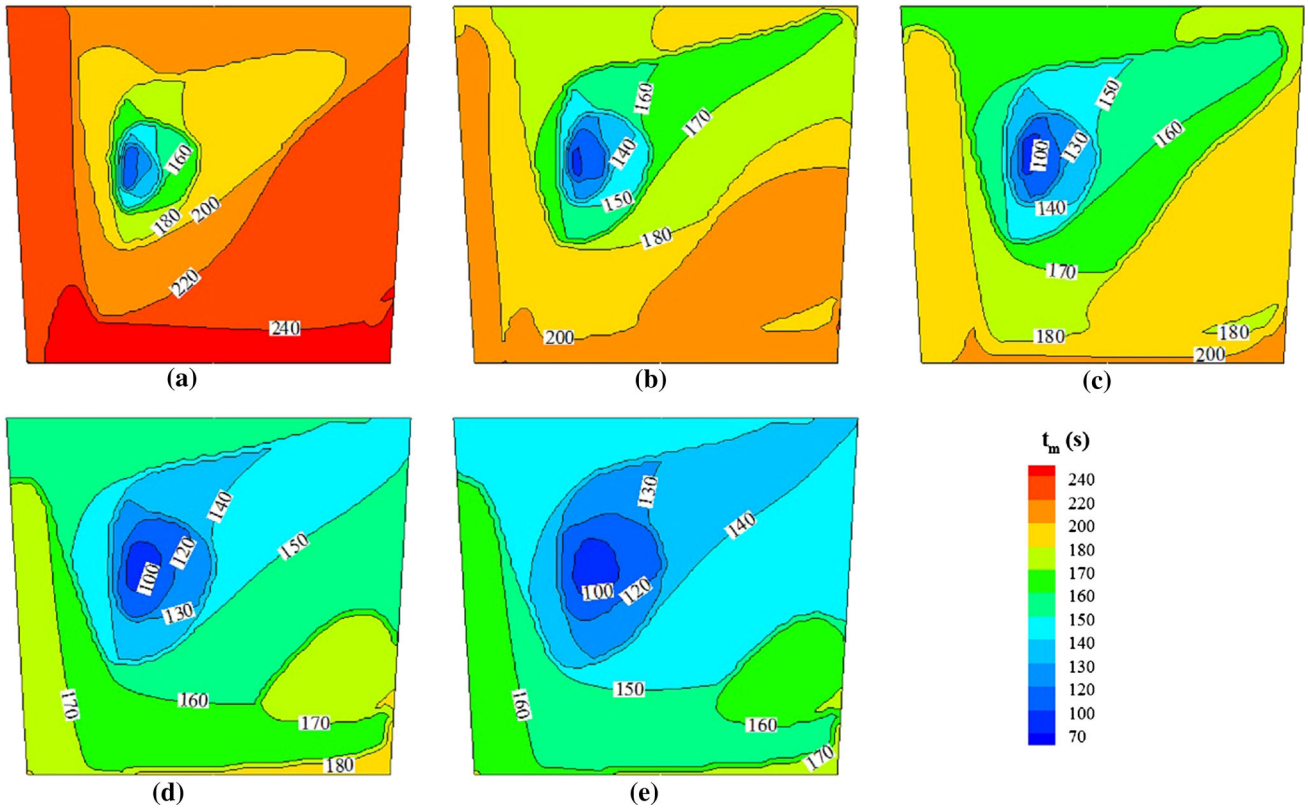

Fig. 9—Predicted mixing time map in the vertical plane of 150-ton gas-stirred ladle at different gas flow rates. (*a*) 120 NL/min, (*b*) 170 NL/min, (*c*) 220 NL/min, (*d*) 270 NL/min, (*e*) 320 NL/min.

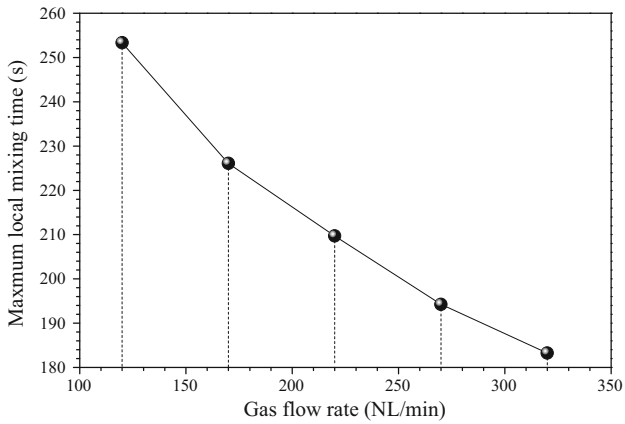

Fig. 10—Effect of gas flow rate on mixing time.

The superscript "bottom" means the bottom of the ladle where gas bubbles are injected, and the subscript "0" refers to the standard temperature and pressure (STP) of 273.15 K and 101,325 Pa. H is the bath depth; y_i is the vertical coordinate starting from the bottom of the ladle (m).

When argon bubbles are injected from the porous plug, the bubble size distribution is also taken into account in this model. The spectrum of bubble size can be described by the following logarithmic normal function[4]:

$$P = P_{\mathrm{m}} \exp\left(\frac{-\left[\ln(d_{\mathrm{b}}) - \ln(d_{\mathrm{b}}^{\mathrm{m}})\right]^2}{2[\ln(s)]^2}\right) \quad [28]$$

$$d_{\mathrm{b}}^{\mathrm{m}} = 0.04\left(\frac{Q_{\mathrm{b}}^2}{g}\right)^{0.2} + 0.0007 \quad [29]$$

where P_{m} is the maximum relative probability; $d_{\mathrm{b}}^{\mathrm{m}}$ is the bubble diameter with the maximum number distribution (m); and s is the standard deviation, equal to 0.026 m based on the calibration to match the Wood's metal experiment.

The maximum bubble diameter is assumed to be 50 pct of the value evaluated from Davidson and Schtiler[47] based on the Wood's metal experiment[4]:

$$d_{\mathrm{b}}^{\mathrm{N}} = 0.69\left(\frac{Q_{\mathrm{b}}^2}{g}\right)^{0.2} \quad [30]$$

B. *Ferroalloy Melting and Mixing*

The ferroalloy melting and mixing processes are also modeled after the fluid flow is predicted. The ferroalloy is first treated as spherical particles and added into the

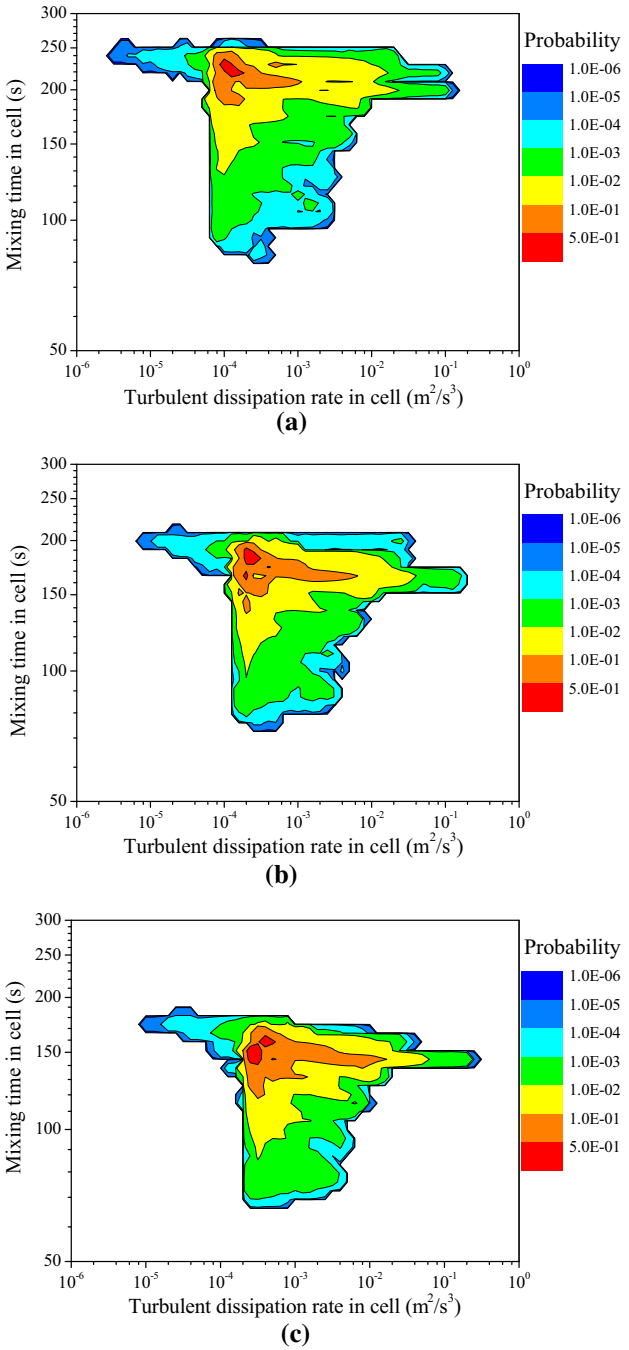

Fig. 11—Relationship between turbulent dissipation rate and mixing time in computational cells for different gas flow rates. (*a*) 120 NL/min, (*b*) 220 NL/min, (*c*) 320 NL/min.

ladle just above the porous plug. Then, the ferroalloy particles are coated by solidified steel shells due to the frozen liquid, and the particles then travel through the flow field. After a period of melting time, each ferroalloy particle melts and turns into a mass source of solute. The species transport model is used to describe the diffusion of dissolved solute. Finally, the local mixing time in the whole ladle is predicted based on its definition.

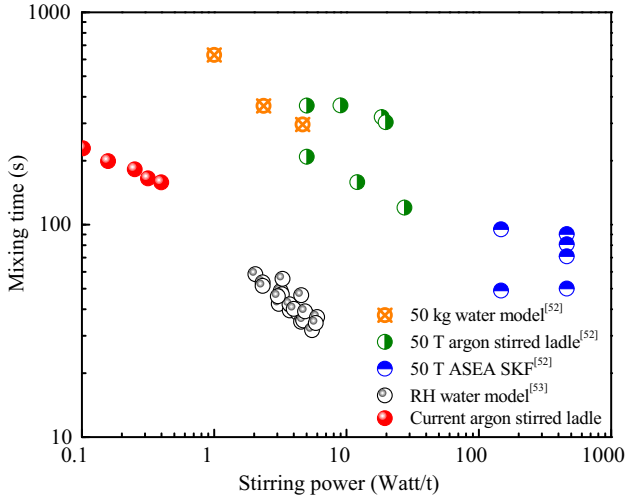

Fig. 12—Mixing time as a function of stirring power.

After the quasi-steady state of fluid flow is reached, FeMn ferroalloy containing 71.8 wt pct Mn is added into the liquid steel directly above the porous plug where the slag layer is thinner than the rest of the top surface. It takes 6 seconds to add 435.24 kg of ferroalloy to the steel at a constant mass flow rate of 72.54 kg/s. For simplicity, the ferroalloy is assumed to be spherical particle with the diameter of 30 mm and added in a 200 mm diameter circle region centered in the eye above the porous plug. The initial velocity of each ferroalloy particle entry into the liquid steel is set to 6.26 m/s vertically downward, corresponding to a two-meter vertical free fall velocity.

When cold ferroalloy enters into the molten steel, a solidified steel shell is formed around the surface of the ferroalloy particle. Thus, the transport of ferroalloy particle is treated as discrete phase particle which is calculated using the same equations as those for gas bubbles, except that the ferroalloy particle is assumed to be spherical and the spherical drag law is applied:

$$C_{D,A} = a_1 + \frac{a_2}{Re_A} + \frac{a_3}{Re_A^2} \quad [31]$$

where the constants a_1, a_2, and a_3 are given by Morsi and Alexander.[48]

During the transport process, ferroalloy particles are heated by the surrounding liquid, and when the shell disappears the center is liquid because FeMn melts at about 1488 K. Thus, the molten ferroalloy is suddenly introduced into the liquid as a mass source of solute and diffuses from the position where the steel shell disappears. The duration of the solidified shell existence can be calculated according to the model of Zhang and Oeters.[43]

$$t = \frac{\rho_A C_{p,A} d_A}{2\pi h} \frac{T_S - T_0}{T_M - T_S} \quad [32]$$

where t is the shell existence time (s); ρ_A is the density of ferroalloy; $C_{p,A}$ is the heat capacity of ferroalloy (J/kg K); d_A is the diameter of ferroalloy particle (m); T_S,

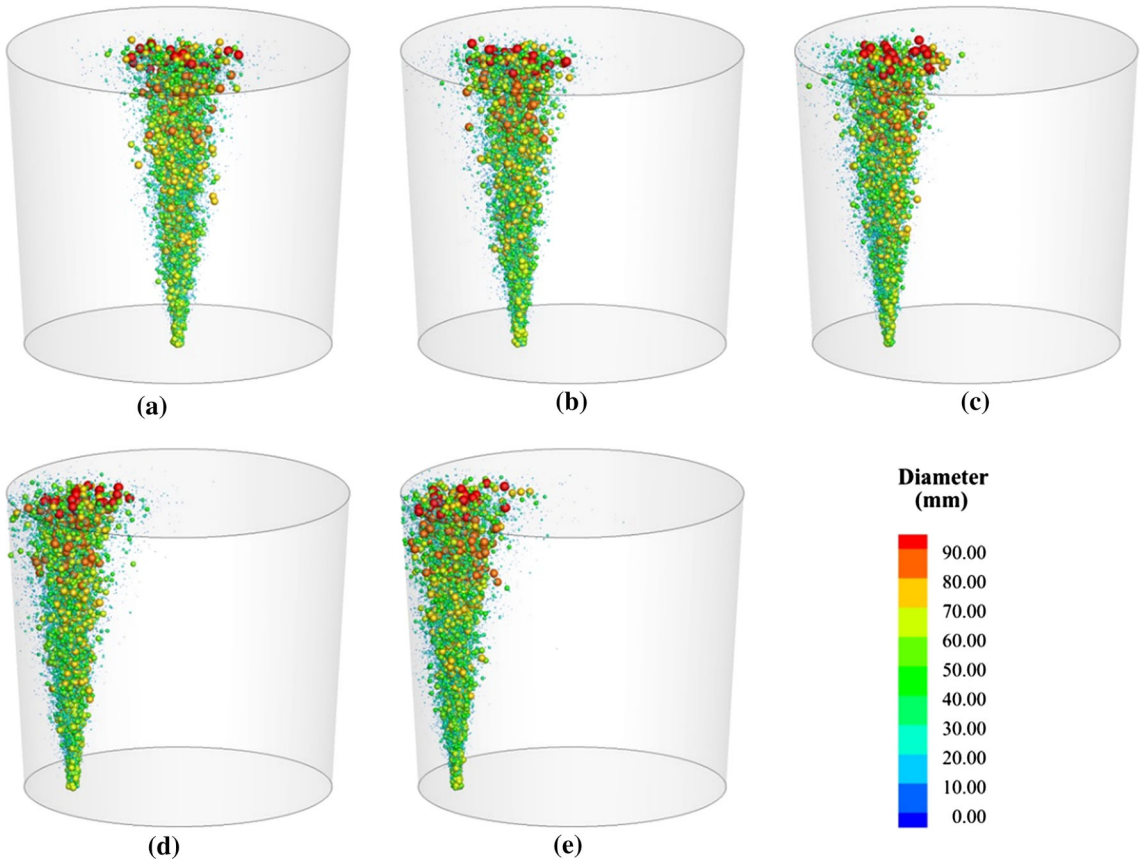

Fig. 13—Predicted bubble distribution in 150-ton gas-stirred ladle with different porous plug locations. (*a*) Center, (*b*) $r/R = 0.34$, (*c*) $r/R = 0.50$, (*d*) $r/R = 0.68$, (*e*) $r/R = 0.75$.

T_M, and T_0 are the solidification temperature of the melt (1803 K), the temperature of the melt (1863 K), and the initial temperature of the ferroalloy particle (298 K), respectively.

The heat transfer coefficient h is estimated from the Nusselt number Nu and the following correlation proposed by Whitaker[49] is employed:

$$\mathrm{Nu} = \frac{d_A h}{k_M} \quad [33]$$

$$\mathrm{Nu} = 2 + \left(0.4\mathrm{Re}_A^{1/2} + 0.06\mathrm{Re}_A^{2/3}\right)\mathrm{Pr}^{0.4} \quad [34]$$

$$\mathrm{Re}_A = \frac{\rho_l d_A \left(\vec{u_l} - \vec{u_A}\right)}{\mu_l} \quad [35]$$

$$\mathrm{Pr} = \frac{C_{p,M}\mu_l}{k_M} \quad [36]$$

where $\vec{u_A}$ is the velocity of ferroalloy particle (m/s); $C_{p,M}$ is the heat capacity of molten steel (J/kg K); and k_M is the thermal conductivity of the molten steel (J/m s K).

The shell thickness of ferroalloy particles is also considered:

$$s = \begin{cases} \frac{\sqrt{\mathrm{Fo}}d_A}{\sqrt{\pi}\mathrm{Ph}(\rho_S/\rho_A)} - \frac{(\mathrm{Bi}\theta_M+1)\mathrm{Fo}d_A}{2\mathrm{Ph}(\rho_S/\rho_A)} & \mathrm{Fo} < 1/\pi \\ \frac{d_A}{2\mathrm{Ph}(\rho_S/\rho_A)}\left(\frac{1}{\pi} - \mathrm{Bi}\theta_M\mathrm{Fo}\right) & \mathrm{Fo} \geq 1/\pi \end{cases} \quad [37]$$

$$\theta_M = \frac{T_M - T_S}{T_S - T_0} \quad [38]$$

$$\mathrm{Bi} = \frac{\mathrm{Nu}k_l}{2k_A} \quad [39]$$

$$\mathrm{Fo} = \frac{4k_A t}{\rho_A C_{p,A} d_A^2} \quad [40]$$

$$\mathrm{Ph} = \frac{\Delta H_S}{C_{p,A}(T_S - T_0)} \quad [41]$$

where s is the thickness of the shell; ρ_S is the density of the steel shell; $C_{p,A}$ is the heat capacity of the ferroalloy; H_S is the enthalpy change of the melting of the shell; k_A is the thermal conductivity of the ferroalloy; θ_M is the

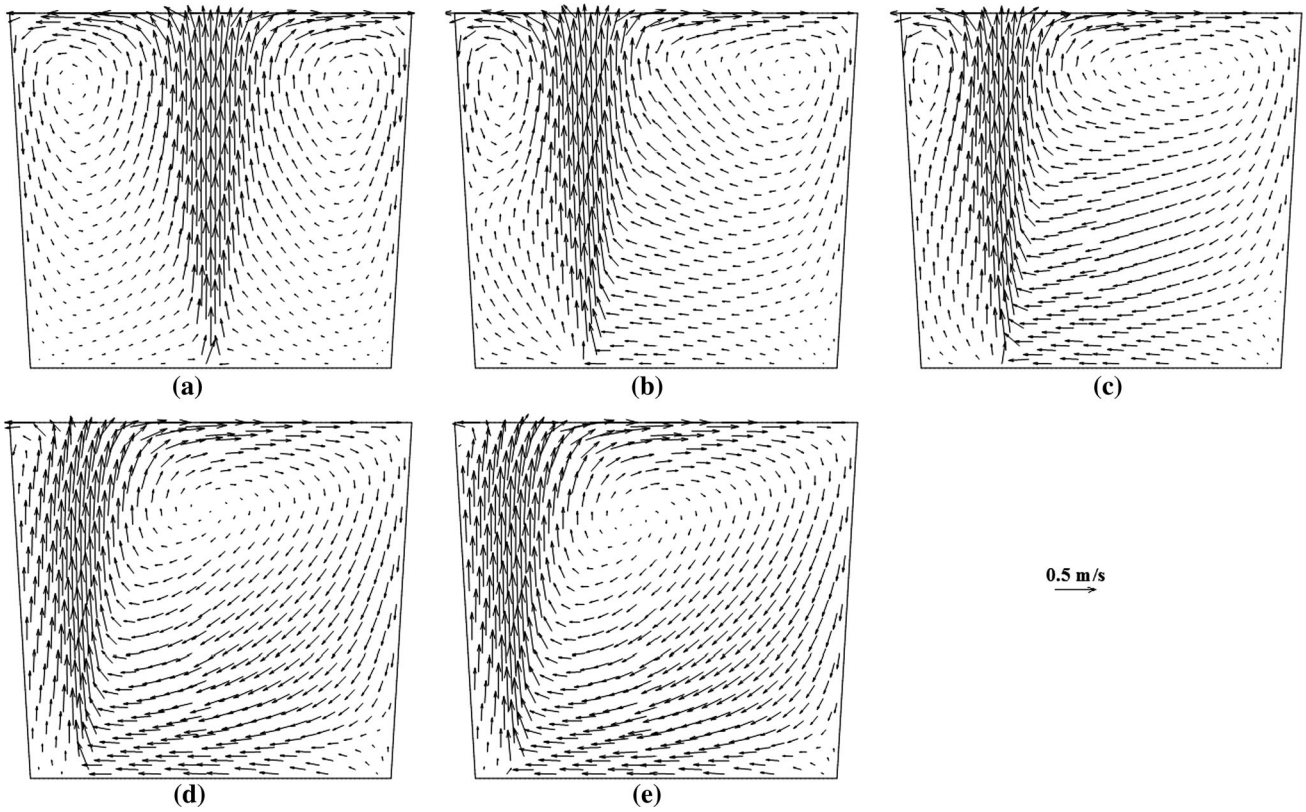

Fig. 14—Predicted velocity field in the vertical plane of 150-ton gas-stirred ladle with different porous plug locations. (*a*) Center, (*b*) $r/R = 0.34$, (*c*) $r/R = 0.50$, (*d*) $r/R = 0.68$, (*e*) $r/R = 0.75$.

dimensionless temperature; Bi, Fo, and Ph and Pr Re are the Biot number, the Fourier number, the phase transfer number, the Prandtl number and the Reynolds number, respectively.

This model indicates that the melting process is greatly affected by such factors as the particle size, the temperature of the melt, and the particle-melt slip velocity.

As the steel shell disappears, the diffusion of dissolved solute is described by the species transport model. The conservation equation in terms of the concentration of dissolved solute is expressed as:

$$\frac{\partial}{\partial t}(\rho C) + \nabla \cdot (\rho u C) = \nabla \cdot \left(\rho D_{\mathrm{M}} + \frac{\mu_{\mathrm{t}}}{Sc_{\mathrm{t}}}\right)\nabla C \qquad [42]$$

where C is the local mass fraction of the solute; D_{M} is the diffusion coefficient of the solute (m^2/s); and Sc_t is the turbulent Schmidt number defined as 0.7.

Mixing time is a very important parameter to evaluate the flow pattern in the gas-stirred ladle. The advantage of the numerical model is its ability to check the mixing criteria and predict the local mixing time in every computational cell. The local mixing time is defined as that time during which the local concentration of ferroalloy element is reached within 5 pct deviation of the homogeneous value. The mixing time of the entire ladle is defined as the maximum local mixing time.

C. *Boundary Conditions and Computational Details*

In the present study, the commercial CFD software Fluent 14.0 combined with a user-defined function (UDF) is used to simulate the fluid flow and ferroalloy mixing in argon-stirred ladles. The parameters of liquid steel, argon gas, and ferroalloy are listed in Table II. The geometry and mesh system are shown in Figure 1 and the optimal number of mesh cells is 384,000.

For the fluid flow simulation, the second-order implicit time discretization scheme is used for the unsteady calculation with a chosen time step of 0.005 seconds. The PISO scheme is used for the pressure–velocity coupling. The convergence criteria are set to 10^{-5} for the residuals of the continuity equation, the momentum equations, and the transport equations of k and . A non-slip boundary condition is used at the bottom and sidewalls, and the standard wall function is used to model the turbulence characteristic in the near-wall region. Argon bubbles are injected through a porous plug or two plugs set at the bottom of the ladle. The diameter of the porous plug is 100 mm. The top surface is set as free shear condition, and argon bubbles are assumed to escape from the top surface. The flowchart of the fluid flow model is shown in Figure 2.

The ferroalloy melting and mixing processes are calculated based on the flow field. Ferroalloy particles are tracked using the discrete phase model (DPM)

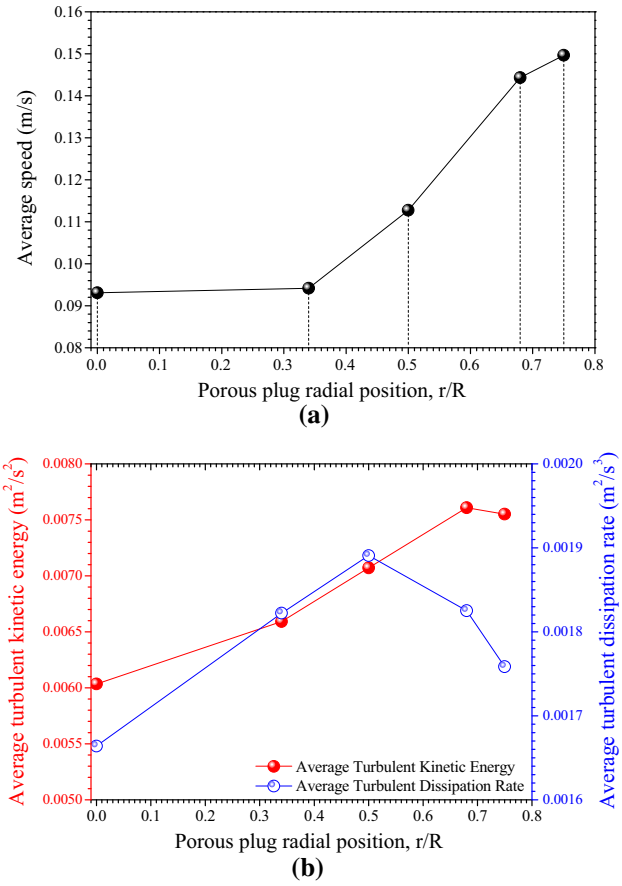

Fig. 15—Effects of porous plug location on (*a*) average speed, (*b*) average turbulent kinetic energy and its dissipation rate.

before melting. During each ferroalloy particle trajectory calculation, the melting time and the trajectory length are recorded using a UDF. Once melted, the ferroalloy particle turns into a mass source of Mn at the melting location, and the species transport model applies. For the species transport model, the zero flux boundary condition is used at the top surface, and bottom and side walls. After the solute Mn uniformly dissolves into the liquid steel, the homogeneous value of Mn equals to 0.2 pct. In order to evaluate the mixing time in the entire ladle, the mixing criteria are checked in every cell using the UDF and the local mixing time is predicted.

III. RESULTS AND DISCUSSION

A. *Effects of Lift Coefficient*

The effects of lift coefficient on the liquid velocity and the bubble volume fraction are analyzed in the current model, as shown in Figure 3. To determine an appropriate lift coefficient, the experimental results obtained by Xie and Oeters[3,4] are also shown in Figure 3. A cylindrical glass vessel with liquid Wood's metal, an internal diameter of 400 mm, a bath height of 370 mm and axis symmetric bottom gas injection was used as the modeling vessel. Nitrogen was used as the modeling gas, and the gas flow rate was 2×10^{-4} Nm^3/s. It is clear that the lift coefficient has a small influence on the liquid vertical velocity; however, it strongly affects the bubble volume fraction. As the lift coefficient increases, the bubble volume fraction in the plume decreases, and the width of the plume increases. This behavior was also reported by Guo and Irons[28] that the lift force was mainly responsible for the bubble spreading from the plume center. Lou and Zhu[22] investigated the effect of lift coefficient on the bubbly plume using the Eulerian–Eulerian approach. It also indicated that the gas phase was gradually clustering near the center and the bubbly plume shape became narrower with the lift coefficient decreased.

B. *Ferroalloy Dissolution and Mixing Process*

The details of the ferroalloy dissolution process and the concentration maps as a function of time for the case of a gas flow rate of 220 NL/min and the porous plug radial position of 0.68*R* are shown in Figure 4. Part (a) corresponds to the moment that the ferroalloy was adding on top of the spout. The spheres represent ferroalloy particles. They penetrate into the liquid steel due to the downward velocity. Meanwhile, ferroalloy particles are coated by solidified steel shells when they are thrown into the liquid steel, and the steel shells are always existing during the movement of ferroalloy particles. Five seconds later it is shown in part (b) how the particles emerge to the top due to the buoyancy caused by the density difference between the liquid steel and the ferroalloy and the fluid flow evolved by the argon injection. Coated by the solidified steel shells, the alloy hardly diffuses before the shell melting. Ferroalloy particles drift along the surface just beneath the slag and accumulate around the perimeter of the top surface opposite from the plume. Part (c) describes the moment when a fraction of the solid particles have been melted. The ferroalloy changes to liquid before the shell disappears since the solidification temperature of ferroalloy is lower than that of the steel and suddenly flows into the liquid steel as a solute where the shell melts and disappears. Thus, ferroalloy particles start to be melted around the perimeter of the top surface opposite from the plume, and the Mn concentration is high at the opposite location of its introduction into the melt. Part (d) represents 30 seconds after the addition was made. It can be shown that the whole ferroalloy is molten and follows a trajectory defined by the recirculation loops. Part (e) describes the concentration profiles after 100 seconds. It is shown a higher concentration in the dead zones. Finally, in part (f) it is shown that manganese has reached full homogenization after 210 seconds. The concentration scale has been normalized to the unity; however, in weight percent, it corresponds to 0.2 pct Mn.

The melting time and the trajectory length of each ferroalloy particle are recorded in this study, as shown in Figure 5. The superheat of the liquid steel is 60 K and the diameter of the ferroalloy is 30 mm. Due to the

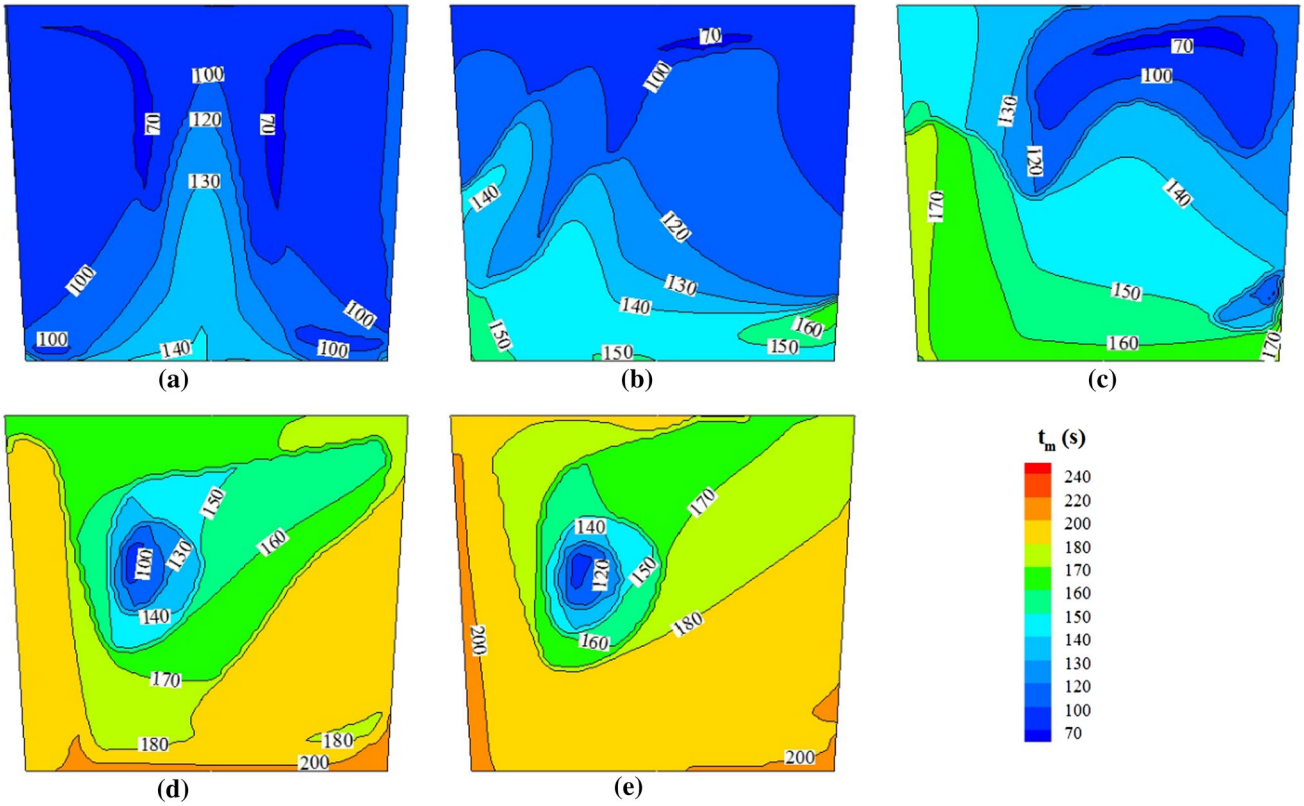

Fig. 16—Predicted mixing time map in the vertical plane of 150-ton gas-stirred ladle with different porous plug locations. (*a*) Center, (*b*) $r/R = 0.34$, (*c*) $r/R = 0.50$, (*d*) $r/R = 0.68$, (*e*) $r/R = 0.75$.

turbulent random walk, the heat transfer is better for the higher particle-melt slip velocity; therefore the ferroalloy particle melts faster. The longest melting time is 12.86 seconds, and the shortest is 6.00 seconds. Even though the ferroalloy particles have an identical diameter, it takes more than twice of melting time for the longest one to the shortest. The trajectory length is in the range of 4.16 to 6.66 m and the average trajectory length is 5.99 m. It should be noticed that more than 90 pct of ferroalloy particles are traveled between 5.6 and 6.4 m.

C. *Effects of Gas Flow Rate*

The effects of gas flow rate on the bubble size distribution, velocity fields, mixing and dissolution of ferroalloys are analyzed for a fixed porous plug radial position of 0.68*R*. The bubble size distributions in the liquid at different gas flow rates are shown in Figure 6. As the gas bubble rises upward, its volume expands because of the lower ferrostatic pressure. The bubble size also becomes bigger by increasing the gas flow rate. The bubble size increases from 36 mm, on average, when the gas flow rate is 120 NL/min to 51 mm when the gas flow rate increases to 320 NL/min. Figure 7 shows the effect of gas flow rate on the average velocity of liquid steel. It is shown an increase in the average velocity as the gas flow rate increases; from 0.117 to 0.164 m/s with an increment in the gas flow rate from 120 to 320 NL/min, at the same time, the average turbulent kinetic energy and the average turbulent dissipation rate also increases from 5.0×10^{-3} to 10.0×10^{-3} m^2/s^2 and 1.1×10^{-3} to 2.5×10^{-3} m^2/s^3, respectively, which is an indication that the flow becomes more turbulent. The flow pattern with one porous plug located off-center produces two recirculation loops, one of them bigger as the position gets closer to the walls, as shown in Figure 8. It is important to notice that in this configuration, the smallest velocities are reached at the

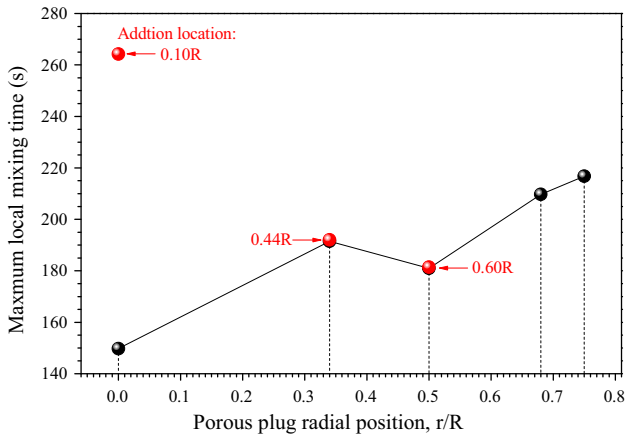

Fig. 17—Effect of porous plug location on mixing time.

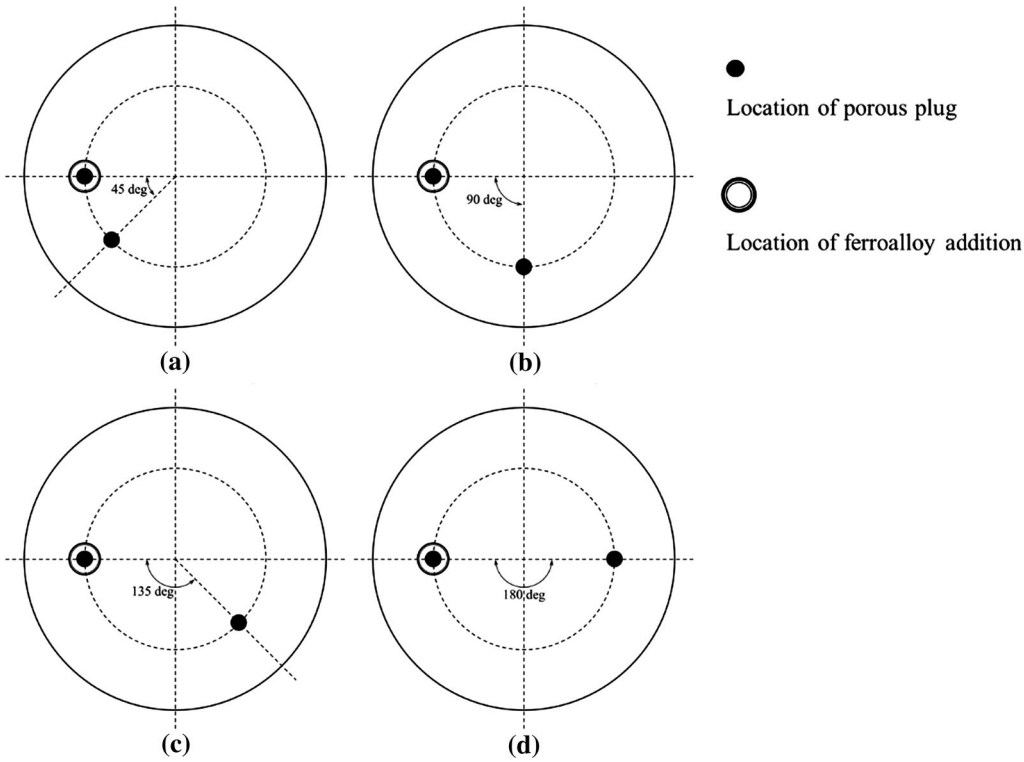

Fig. 18—Details of four different separation angles of two porous plugs in the ladle. (*a*) $\theta = 45$ deg, (*b*) $\theta = 90$ deg, (*c*) $\theta = 135$ deg, (*d*) $\theta = 180$ deg.

opposite side of the location of the porous plug, at the ladle bottom, approximately 0.002 m/s.

Mixing time is related with the velocity fields, therefore the dead zones define its final value. Figure 9 displays mixing time maps for the whole computational domain. It can be observed a faster mixing process in the central part region adjacent to the plume. It should be noticed that the velocity is lower in this region. The mixing of the ferroalloy is controlled by two aspects: the diffusion of the ferroalloy and the transport phenomena. Even though the velocity is lower in this region, the diffusion will also promote the mixing. On the other hand, the velocity is higher in the vicinity of this region, and it facilitates the transport of the liquid containing the high ferroalloy concentration diffused from the lower velocity region. Thus, the mixing is faster in this region due to the diffusion in the region and the better transport dynamic in the vicinity. The volume of liquid steel that mixes faster increases as the gas flow rate increases. The mixing time for this region is in the order of 70 seconds, in comparison with more than 240 seconds for the final mixing time of the volume in the dead zone, when the gas flow rate is 120 NL/min. This result indicates that a volume in a dead zone can take up to three times longer mixing time in comparison with zones of higher turbulence. In the past, all the previous researches on mixing time have been focused on the longest value and ignored to compare with the volume of liquid steel that reaches full homogenization. This comparison is useful because it can be used to define a new reference to improve the mixing process. What is also relevant of the new mixing time maps is that it will be possible to promote a better understanding of the position of the dead zones in a ladle. The first practical approach to identify dead zones was reported by Narita *et al.*[50] in 1971. In accordance with their suggestions, if the porous plug is at half radius then the dead zone is located at the opposite and bottom part of the ladle. The results shown in the mixing time maps of Figure 9 are in agreement with this suggestion; however, it a second dead zone located in the minor recirculation loop can also be observed. Therefore, the use of mixing time maps will improve our current understanding of the location of dead zones for a given set of gas-injection conditions. The true mixing time is a single value for the entire computational domain. This value corresponds to the maximum mixing time. Figure 10 shows the maximum mixing time as a function of gas flow rate. It is clearly shown a decrease in mixing time as the gas flow rate increases, from 253 to 183 seconds by increasing the gas flow rate from 120 to 320 NL/min, respectively. The criterion employed to measure mixing time in this work was 95 pct homogenization in the whole computational domain. Warzecha *et al.*[51] carried out experiments to determine the mixing time in a 138-ton gas-stirred ladle and reported the mixing time ranging between 173 and 183 s for the gas flow rate of 200 NL/min. Aoki *et al.*[41] investigated the mixing phenomena in a 100-ton gas-stirred ladle both experimentally and theoretically and found that the mixing times ranged from 88 to 187 seconds for the gas flow rate of 170 NL/min depending on the definition and location of mixing. Clearly, the

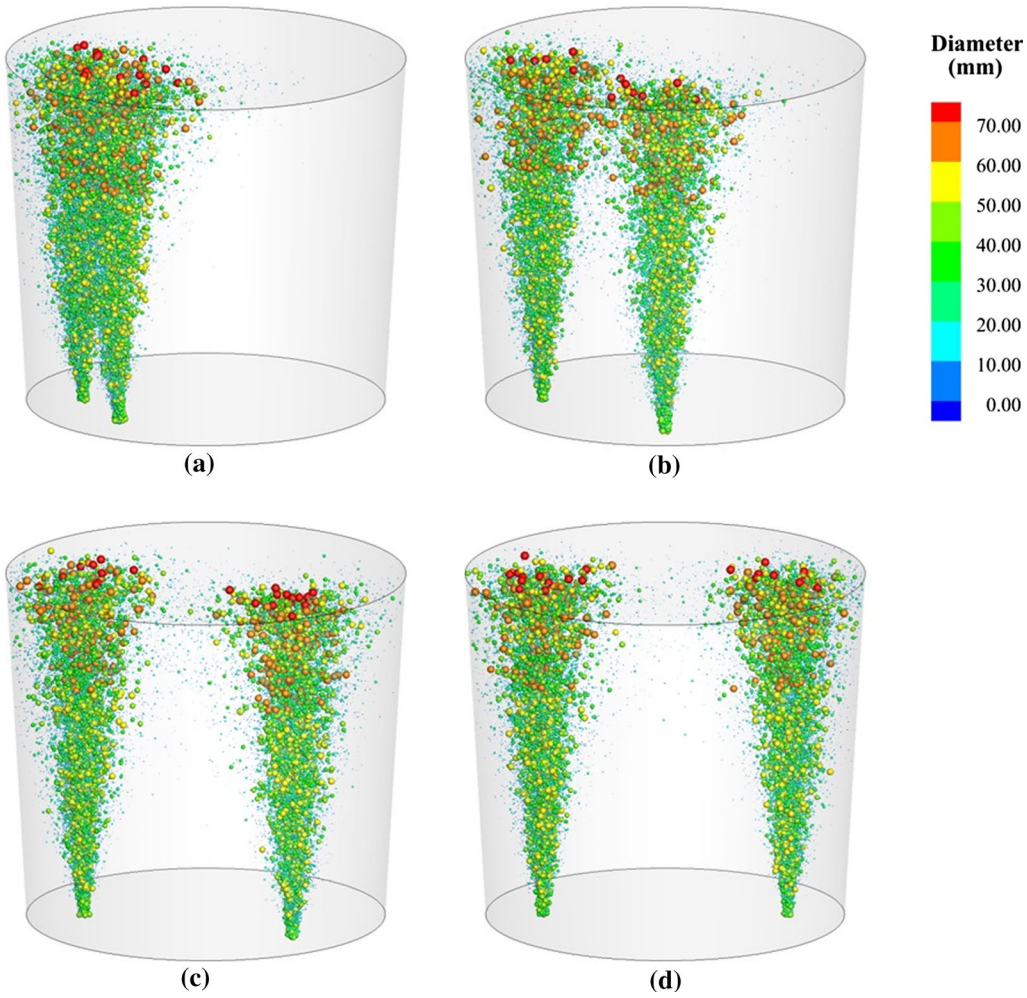

Fig. 19—Predicted bubble distribution in 150-ton gas-stirred ladle with different separation angles. (*a*) $\theta = 45$ deg, (*b*) $\theta = 90$ deg, (*c*) $\theta = 135$ deg, (*d*) $\theta = 180$ deg.

calculated mixing time in the current study closely approximates to that reported by Warzecha *et al.*[51] and Aoki *et al.*[41]

The relationship between the turbulent dissipation rate and the mixing time in computational cells for different gas flow rates is shown in Figure 11. In order to clearly exhibit this relationship, the counter map is used, in which the probability represents the number of cells located in the region. It is observed that the maximum probability region corresponds to the turbulent dissipation rate of 1.0×10^{-4}, 2.5×10^{-4} and 4.0×10^{-4} m^2/s^3 and the mixing time of 230, 182 and 158 seconds, for the gas flow rate of 120, 220 and 320 NL/min, respectively.

The dependence of the mixing time on the stirring power is shown in Figure 12, which also includes results reported by Nakanishi *et al.*[52] and Zhang and Li.[53] The stirring power is converted from the turbulent dissipation rate using the dimensional analysis, and the maximum probability region in Figure 11 is adopted. The well-known relationship between the mixing time and the stirring power is obtained: mixing time decreases with increasing the stirring power. Even though the stirring power in the current study is smaller than those reported in the literature, the relationship between the stirring power and the mixing time is similar.

D. *Effects of Porous Plug Radial Position*

The effects of porous plug radial position, from $0.34R$ to $0.75R$, on the bubble size distribution, velocity fields, mixing and dissolution of ferroalloys are analyzed for a fixed gas flow rate of 220 NL/min. The effect of porous plug radial position on the bubble size distribution in the liquid is shown in Figure 13. The bubble diameter is not affected by the position of the porous plug; however, the results are important to show the Coanda effect.[54,55] This effect pulls the rising bubbles to the walls, especially when the porous plug radial position is closer to the walls, enhancing the hydrodynamic erosion of the ladle's refractories. At the porous plug radial position of $0.68R$ the plume makes contact with the ladle's walls. This position indicates a transfer of kinetic energy from the rising bubbles to the walls, affecting the mixing efficiency of liquid steel.

The effect of porous plug radial position on the velocity profiles is shown in Figure 14. It is observed

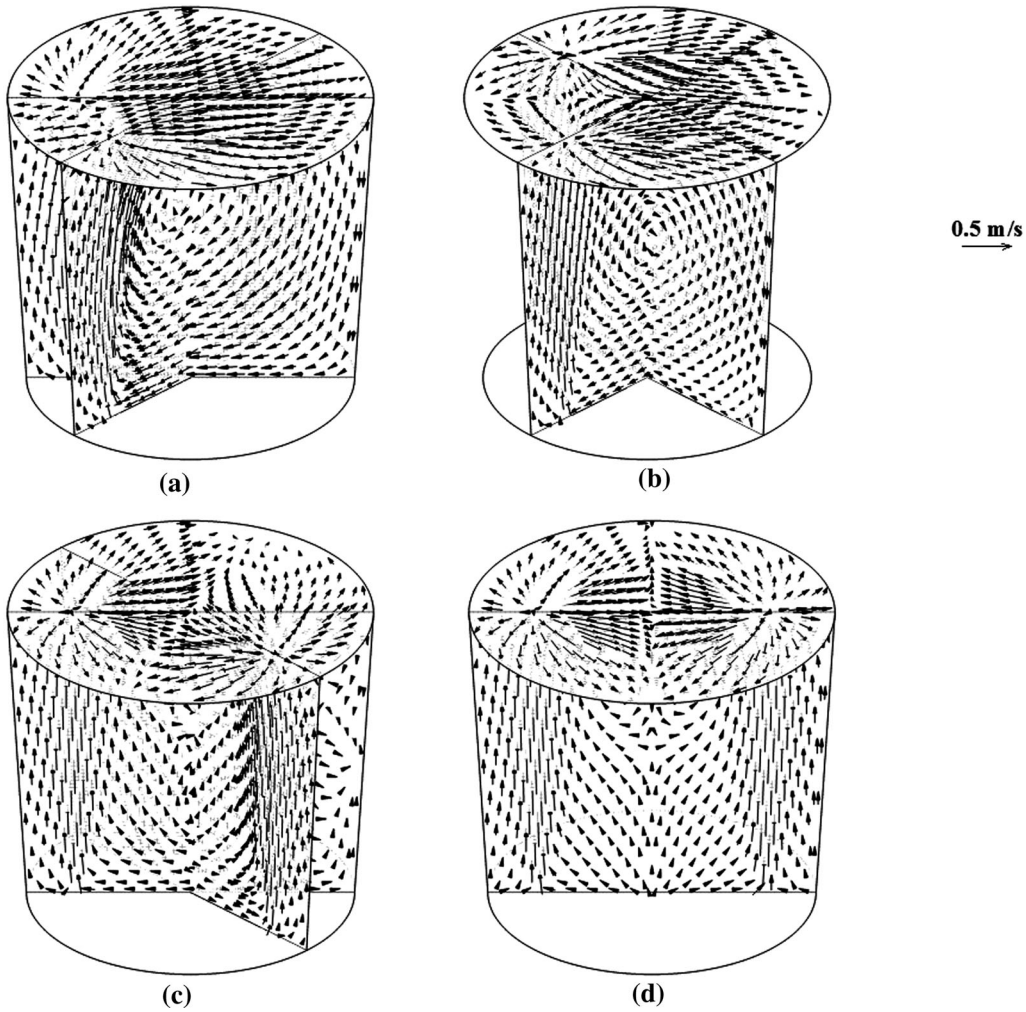

Fig. 20—Predicted velocity field in 150-ton gas-stirred ladle with different separation angles. (*a*) $\theta = 45$ deg, (*b*) $\theta = 90$ deg, (*c*) $\theta = 135$ deg, (*d*) $\theta = 180$ deg.

that one porous plug creates two recirculation loops. When the porous plug is centrally located, the two recirculation loops are symmetrical; however, as the porous plug moves to the ladle walls, one recirculation loop gets bigger and the other one smaller. In this process, the average velocity increases, from 9.3×10^{-2} to 14.4×10^{-2} m/s, when the radial position changes from the center to 0.68*R*, respectively, as shown in Figure 15 (a). In this figure, a subsequent increase from 0.68*R* to 0.75*R* also produces a small increase in the average velocity to 14.9×10^{-2} m/s of the liquid in spite of the energy released from the bubbles to the walls. The loss in stirring energy, as the porous plug gets closer to the walls is illustrated in Figure 15(b) because the average turbulent kinetic energy decreases when the porous plug is moved from the radial position 0.68 to 0.75*R*.

The behavior of mixing time as a function of porous plug radial position is analyzed with maps on mixing time showed in Figure 16 and the maximum mixing time values showed in Figure 17. It is observed that the shortest mixing time is obtained for central gas injection in contradiction with most previous research work.[14,24] A detailed analysis of this behavior shows that central gas injection is extremely sensitive to the point of addition. This behavior was also reported by Zhu *et al.*[14] attributing this phenomenon to a low value of the azimuthal velocity component. If the porous plug is placed in the center but the addition is made at any point of the ladle eye, except in the exact central part of the ladle eye, mixing time increases dramatically. In our calculations, mixing time increases from 150 seconds when the addition is made in the center to 265 seconds if the addition is made at a radial position of 0.10*R*. On the other hand, for an eccentric porous plug position, mixing time is not so sensitive to changes in the addition position. The results for porous plug radial positions at 0.34 and 0.50*R* and different additions positions provide similar values on mixing time. Zhu *et al.*[14] indicated that for an eccentric position of the porous plug, the azimuthal velocity component is larger. In Figure 17, mixing time for the axis-symmetric gas injection has different values corresponding to different points of addition of the ferroalloy. In addition, it can be found from Figure 16 that the maximum local mixing time is

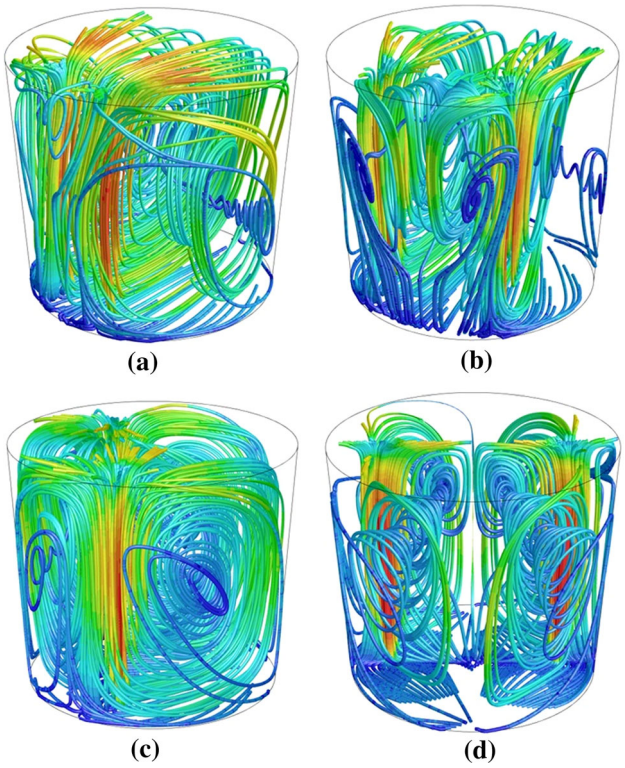

Fig. 21—Predicted recirculation loop in 150-ton gas-stirred ladle with different separation angles. (*a*) $\theta = 45$ deg, (*b*) $\theta = 90$ deg, (*c*) $\theta = 135$ deg, (*d*) $\theta = 180$ deg.

located at the bottom center of the ladle for the central gas injection, while it is situated at the bottom near the ladle wall for the eccentric injection. Taking into consideration that an off-center addition with a porous plug located in the center is a common practice, it is then estimated a large value on mixing time, and therefore it is then obtained an optimal value on the porous plug radial position that reaches the shortest mixing time. The results on Figure 17 would suggest that the optimal value is 0.50*R*, although, this radial position doesn't report the maximum average velocity, it reports the maximum average turbulent dissipation rate, as shown in Figure 15(b).

E. *Effects of Separation Angle*

The effects of separation angle on the bubble size distribution, velocity fields, mixing, and dissolution of ferroalloys are analyzed for a fixed gas flow rate of 220 NL/min and porous plug radial position of 0.68*R*. The arrangement of the different separation angles (θ) is shown in Figure 18. It is important to notice the same radial position in both porous plugs. The effect of porous plug separation angle on the bubble size distribution in the liquid is shown in Figure 19. The separation angle has no effect on the bubble size. Plume interaction is easily observed at different separation angles, for example as the separation angle decreases from 180 to 45 deg it is observed that both plumes start to interact when the separation angle reaches 90 deg.

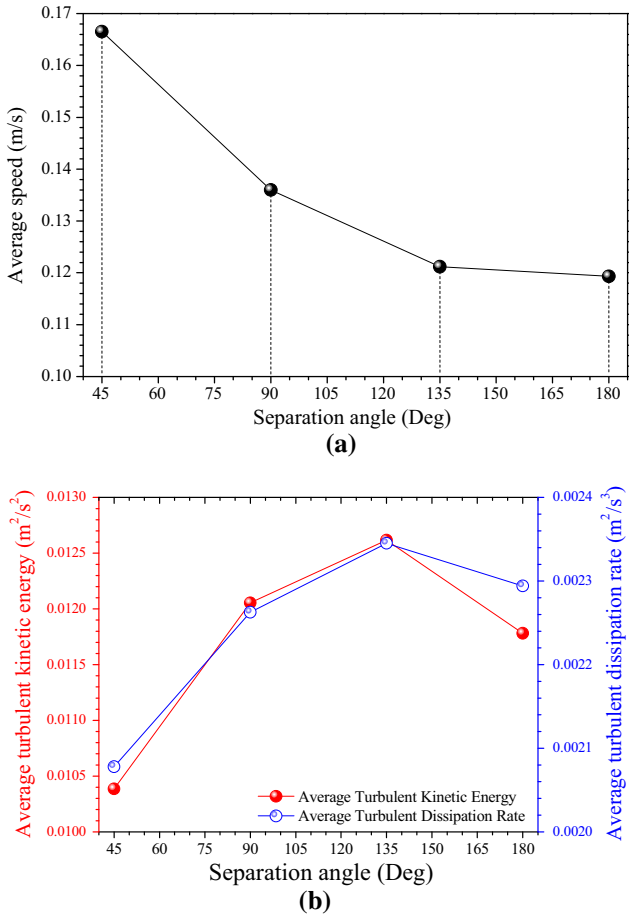

Fig. 22—Effect of separation angle on (*a*) average speed, (*b*) average turbulent kinetic energy and its dissipation rate.

This interaction is related with the formation of one single plume as the rising bubbles from each plume collide during its vertical motion. The extent of this collision has a significant effect on mixing phenomena as can be shown in Figure 20. This figure indicates different flow patterns as a function of the separation angle. When the separation angle is 45 deg, the two plumes collide, emerge with a larger plume that forms a large recirculation rate. The volume of liquid within the separation angle of 45 deg forms two small recirculation loops of high turbulence with collisions among streamlines. For a separation angle of 90 deg, there is also the formation of three recirculation loops. The two smaller recirculation loops are located in the angle of 45 deg that separates the two porous plugs. If the separation angle is now increased to 135 deg it appears the formation of four recirculation loops. The new recirculation loop involves additional collisions causing a decrease in the average velocity. The extent of those collisions is even greater for a separation angle of 180 deg with the formation of four symmetric recirculation loops. Figure 21 provides a different perspective of the recirculation loops as a function of the separation angle. The streamlines are clearly illustrated in these figures. The decrease in the average velocity as the separation angle increases is shown in Figure 22(a). In this figure, it is

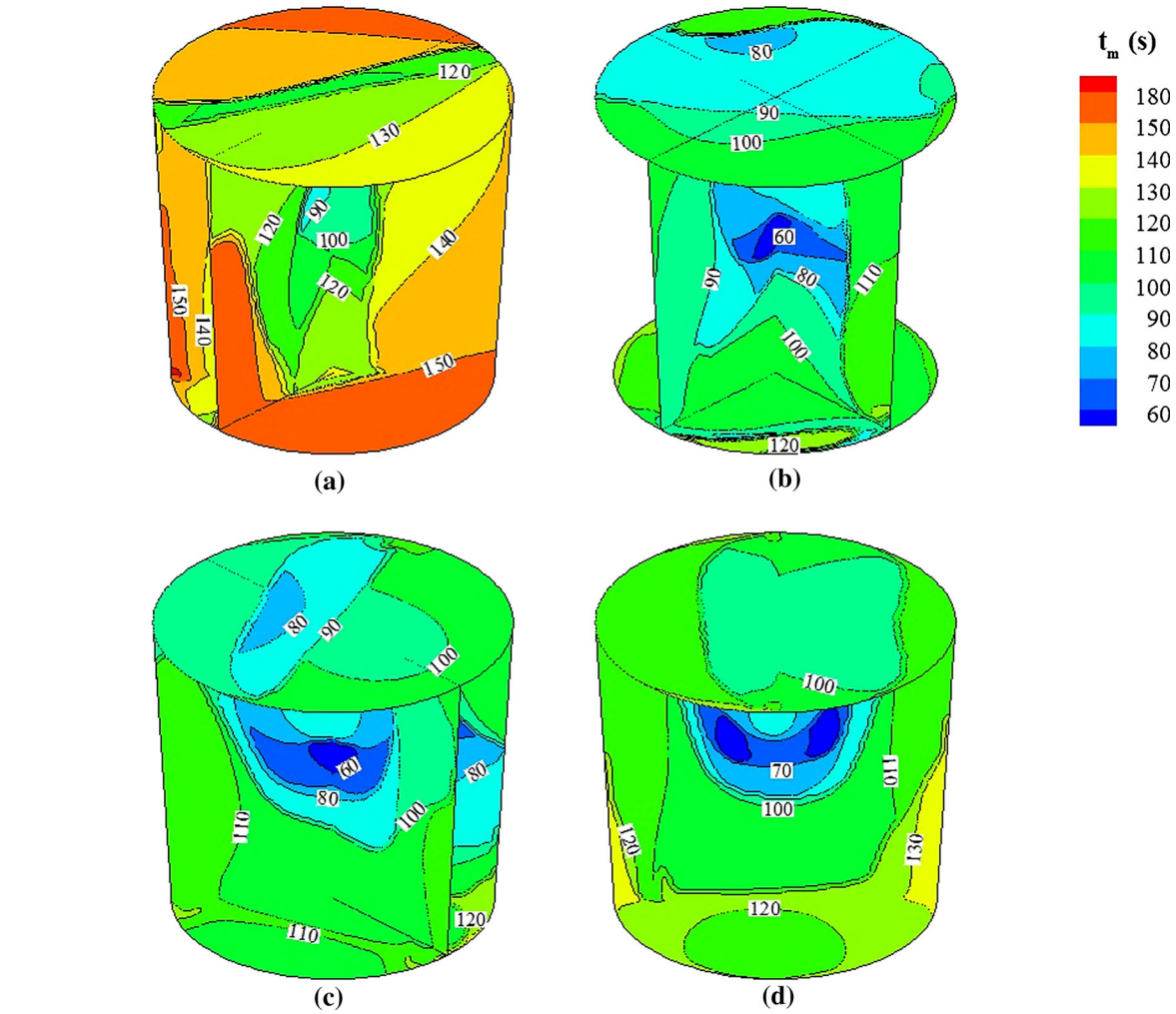

Fig. 23—Predicted mixing time map in 150-ton gas-stirred ladle with different separation angles. (*a*) $\theta = 45$ deg, (*b*) $\theta = 90$ deg, (*c*) $\theta = 135$ deg, (*d*) $\theta = 180$ deg.

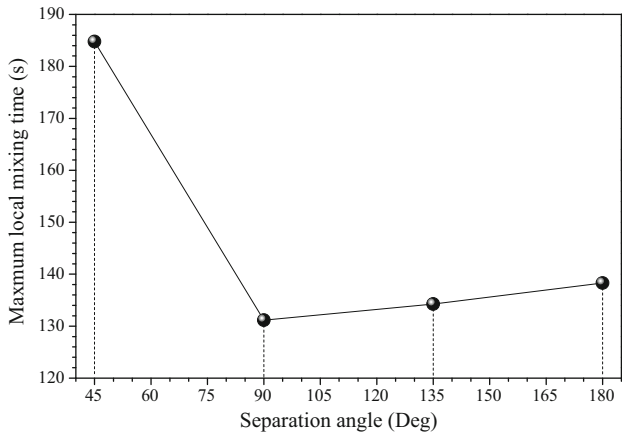

Fig. 24—Effect of separation angle of two porous plugs on mixing time.

observed that the average velocity decreases from approximately 0.17 to 0.12 m/s when the separation angle increases from 45 to 180 deg. On the other hand, the average turbulent kinetic energy, and its dissipation rate increases as the separation angle increases, as shown in Figure 22(b). This is due to a more uniform distribution of the kinetic energy throughout the ladle. The collisions between recirculation loops when the separation angle is 180 deg contribute to a decrease in the average turbulent kinetic energy and the average turbulent dissipation rate.

The previous results in regard to changes in separation angle with fixed values on the gas flow rate and porous plug radial positions indicate a complex flow structure. On the one hand, by increasing the separation angle, the average velocity decreases, and at the same time, the turbulence parameters increase. This behavior has been explained in terms of the collisions among the different recirculation loops that are created. The two opposing effects lead to the presence of a critical separation angle that provides more efficient mixing conditions. Figure 23 reports maps on mixing time, and Figure 24 shows the maximum mixing time, as a function of the separation angle. It is observed that the shortest mixing time is reached with a separation

angle of 90 deg, approximately 131 seconds; however, the difference in mixing time with still larger separation angles, say 135 and 180 deg, is small. For a separation angle of 180 deg, the mixing time is approximately 138 seconds. A comparison of mixing time with one and two nozzles for the same gas flow rate of 220 NL/min and a radial position of 0.68*R* indicates better mixing conditions with two porous plugs, independent of the separation angle. Mixing time with one porous plug takes 210 seconds, and with two porous plugs, even for the worst case with a separation angle of 45 degm takes 185 seconds. The mixing efficiency increases by 66 pct using a separation angle of 90 deg.

Previous investigations related to the optimal separation angle with two porous plugs and symmetric positions have reported different values.[23,39,40] Chen *et al*.[40] investigated a large range of separation angles, from 15 to 135 deg indicating an optimal value of 45 deg. Geng *et al*.[39] reported an optimal value of 180 deg, and more recently, Lou and Zhu[23] reported an optimal value of 90 deg. The large discrepancies in these previous results are attributed to two main factors: (i) many process variables affect mixing time, and a direct comparison is not adequate if the configuration of the injection system is not the same, and (ii) only a few previous investigations have included the top slag layer. The top slag layer has a strong influence on mixing time.

IV. CONCLUSIONS

Based on the Eulerian–Lagrangian approach, a three-dimensional multiphase flow model has been developed to describe the argon-stirred system in steelmaking ladles. The ferroalloy mixing phenomena was also modeled after the fluid flow reaches quasi-steady state. Local mixing time was predicted in the entire computational domain by checking the mixing criteria in every cell. The effects of gas flow rate, porous plug location, and separation angle on the fluid flow and the mixing phenomena were studied, and the following conclusions have been reached:

(1) A novel representation to describe the local mixing time in the entire industrial ladle has been reported using mixing time maps. These maps provide information to identify the location of the dead zones and can be used to compare the chemical stratification during the mixing process; furthermore, it is possible to visualize the mixing efficiency in different regions of the ladle for a given configuration of the porous plugs.
(2) The melting and dissolution processes of ferroalloys have been incorporated in this model. During the melting process, the melting time and the trajectory length of each ferroalloy particle are recorded. For the dissolution process, it is possible to have a precise definition of the concentration fields as a function of time for a given set of injection conditions. It has been found that the concentration fields follow trajectories defined by the recirculation loops.
(3) An increase in the gas flow rate increases the bubble diameter.
(4) It has been confirmed that central gas injection is highly sensitive to the point of addition, in contrast to eccentric gas injection.
(5) The optimal porous plug radial position with one porous plug was obtained for a value of 0.50*R*. This position provides the largest value on the average turbulent dissipation rate.
(6) The optimal separation angle that provides an improved mixing efficiency with two porous plugs was found to be 90 deg. The mechanism that controls this optimal value is attributed to the interaction between recirculation loops. An improved mixing efficiency is reached when the collision of streams of liquid steel from different recirculation loops is decreased.

ACKNOWLEDGMENTS

The authors are grateful for the support from the National Key R&D Program of China (2017YFB0304000 and 2017YFB0304001), the National Science Foundation China (Grant Nos. 51725402, 51504020, and 51704018), the Fundamental Research Funds for the Central Universities (Grant Nos. FRF-TP-15-001C2, FRF-TP-15-067A1, FRF-TP-17-039A1 and FRF-BD-17-010A), Guangxi Key Research and Development Plan (Grant No. AB17129006), the National Postdoctoral Program for Innovative Talents (Grant No. BX201700028), the Beijing Key Laboratory of Green Recycling and Extraction of Metals (GREM) and the High Quality steel Consortium (HQSC), and Green Process Metallurgy and Modeling (GPM^2) at the School of Metallurgical and Ecological Engineering at the University of Science and Technology Beijing (USTB), China.

REFERENCES

1. L. Zhang and B.G. Thomas: *ISIJ Int.*, 2003, vol. 43, pp. 271–91.
2. S. Kim and R. Fruehan: *Metall. Trans. B*, 1987, vol. 18B, pp. 381–90.
3. Y. Xie and F. Oeters: *Steel Res. Int.*, 1992, vol. 63, pp. 93–104.
4. Y. Xie, S. Orsten, and F. Oeters: *ISIJ Int.*, 1992, vol. 32, pp. 66–75.
5. A. Conejo, S. Kitamura, N. Maruoka, and S. Kim: *Metall. Mater. Trans. B*, 2013, vol. 44B, pp. 914–23.
6. D. Mazumdar and R.I.L. Guthrie: *Metall. Mater. Trans. B*, 1994, vol. 25B, pp. 308–12.
7. J. Szekely, H. Wang, and K. Kiser: *Metall. Trans. B*, 1976, vol. 7B, pp. 287–95.
8. T. Roy and A. Majumdar: *JOM*, 1981, vol. 33, pp. 42–47.
9. Y. Sahai and R. Guthrie: *Metall. Trans. B*, 1982, vol. 13B, pp. 193–202.
10. A. Castillejos, M. Salcudean, and J. Brimacombe: *Metall. Trans. B*, 1989, vol. 20B, pp. 603–11.
11. J. Woo, J. Szekely, A. Castillejos, and J. Brimacombe: *Metall. Trans. B*, 1990, vol. 21B, pp. 269–77.
12. S. Joo and R.I.L. Guthrie: *Metall. Trans. B*, 1992, vol. 23B, pp. 765–78.
13. M. Zhu, T. Inomoto, I. Sawada, and T. Hsiao: *ISIJ Int.*, 1995, vol. 35, pp. 472–79.

14. M. Zhu, I. Sawada, and N. Yamasaki: *ISIJ Int.*, 1996, vol. 36, pp. 503–11.
15. M. Madan, D. Satish, and D. Mazumdar: *ISIJ Int.*, 2005, vol. 45, pp. 677–85.
16. H. Turkoglu and B. Farouk: *ISIJ Int.*, 1991, vol. 31, pp. 1371–80.
17. L. Zhang: *Model. Simul. Mater. Sci.*, 2000, vol. 8, pp. 463–75.
18. J.L. Xia, T. Ahokainen, and L. Holappa: *Scand. J. Metall.*, 2001, vol. 30, pp. 69–76.
19. G. Venturini and M. Goldschmit: *Metall. Mater. Trans. B*, 2007, vol. 38B, pp. 461–75.
20. B. Li, H. Yin, C. Zhou, and F. Tsukihashi: *ISIJ Int.*, 2008, vol. 48, pp. 1704–11.
21. F.P. Maldonado, M.A. Ramirez, A. Conejo, and C. Gonzalez: *ISIJ Int.*, 2011, vol. 51, pp. 1110–18.
22. W. Lou and M. Zhu: *Metall. Mater. Trans. B*, 2013, vol. 44B, pp. 1251–63.
23. W. Lou and M. Zhu: *ISIJ Int.*, 2014, vol. 54, pp. 9–18.
24. S. Johansen and F. Boysan: *Metall. Trans. B*, 1988, vol. 19B, pp. 755–64.
25. Y. Sheng and G.A. Irons: *Metall. Mater. Trans. B*, 1993, vol. 24B, pp. 695–705.
26. D. Mazumdar and R.I.L. Guthrie: *ISIJ Int.*, 1994, vol. 34, pp. 384–92.
27. Y. Sheng and G.A. Irons: *Metall. Mater. Trans. B*, 1995, vol. 26B, pp. 625–35.
28. D. Guo and G. Irons: *Metall. Mater. Trans. B*, 2000, vol. 31B, pp. 1457–64.
29. M.L.D. Bertodano, R.T. Lahey, and O.C. Jones: *J. Fluids Eng.*, 1994, vol. 116, pp. 128–34.
30. D. Pfleger and S. Becker: *Chem. Eng. Sci.*, 2001, vol. 56, pp. 1737–47.
31. R.F. Mudde and O. Simonin: *Chem. Eng. Sci.*, 1999, vol. 54, pp. 5061–69.
32. C. Mendez, N. Nigro, and A. Cardona: *J. Mater. Process. Technol.*, 2005, vol. 160, pp. 296–305.
33. Y. Pan, M.P. Dudukovic, and M. Chang: *Chem. Eng. Sci.*, 1999, vol. 54, pp. 2481–89.
34. H. Liu, Z. Qi, and M. Xu: *Steel Res. Int.*, 2011, vol. 82, pp. 440–58.
35. S.W.P. Cloete, J.J. Eksteen, and S.M. Bradshaw: *Miner. Eng.*, 2013, vol. 46–47, pp. 16–24.
36. L. Li, Z. Liu, M. Cao, and B. Li: *JOM*, 2015, vol. 67, pp. 1459–67.
37. D. Mazumdar and R.I.L. Guthrie: *ISIJ Int.*, 1995, vol. 35, pp. 1–20.
38. D. Mazumdar and J.W. Evans: *ISIJ Int.*, 2004, vol. 44, pp. 447–61.
39. D. Geng, H. Lei, and J. He: *Int. J. Min. Met. Mater.*, 2010, vol. 17, pp. 709–14.
40. M. Chen, N. Wang, Y. Yao, J. Geng, and K. Xiong: *Steel Res. Int.*, 2007, vol. 78, pp. 468–72.
41. J. Aoki, B. Thomas, J. Peter and K. Peaslee: AISTech 2004, Warrendale, PA, 2004, pp. 1045–56.
42. M. Tanaka, D. Mazumdar, and R.I.L. Guthrie: *Metall. Mater. Trans. B*, 1993, vol. 24B, pp. 639–48.
43. L. Zhang and F. Oeters: *Steel Res. Int.*, 1999, vol. 70, pp. 128–34.
44. J.T. Kuo and G.B. Wallis: *Int. J. Multiph. Flow*, 1988, vol. 14, pp. 547–64.
45. M. Pourtousi, J.N. Sahu, and P. Ganesan: *Chem. Eng. Process.*, 2014, vol. 75, pp. 38–47.
46. M.L.D. Bertodano, R.T.L. Jr, and O.C. Jones: *Int. J. Multiph. Flow*, 1994, vol. 20, pp. 805–18.
47. J.F. Davidson and B.O.G. Schüler: *Trans. Inst. Chem. Eng*, 1960, vol. 38, pp. 335–42.
48. S.A. Morsi and A.J. Alexander: *J. Fluids Mech.*, 1972, vol. 55, pp. 193–208.
49. S. Whitaker: *AICHE J.*, 1972, vol. 18, pp. 361–71.
50. K. Narita, A. Tomita, Y. Hirooka, and Y. Satoh: *Tetsu-to-Hagane*, 1971, vol. 57, pp. 1101–08.
51. W. Marek, J. Jan, W. Piotr, and P. Herbert: *Steel Res. Int.*, 2008, vol. 79, pp. 852–60.
52. K. Nakanishi, J. Szekely, and C. Chang: *Ironmak. Steelmak.*, 1975, vol. 2, pp. 115–24.
53. L. Zhang and F. Li: *JOM*, 2014, vol. 66, pp. 1227–40.
54. M. Iguchi, K. Sasaki, K. Nakajima, and H. Kawabata: *ISIJ Int.*, 1998, vol. 38, pp. 1297–1303.
55. M. Iguchi and O.J. Ilegbusi: *Modeling Multiphase Materials Processes*, Springer, New York, 2011, pp. 41–88.
56. T.D. Roy, A.K. Majumdar, and D.B. Spalding: *Appl. Math. Model.*, 1978, vol. 2, pp. 146–50.
57. M. Salcudean, K.Y.M. Lai, and R.I.L. Guthrie: *Can. J. Chem. Eng.*, 1985, vol. 63, pp. 51–61.
58. M. Salcudean and K.Y.M. Lai: *Numer. Heat Transf A*, 1988, vol. 14, pp. 97–111.
59. H. Turkoglu and B. Farouk: *Metall. Trans. B*, 1990, vol. 21, pp. 771–81.
60. T. Hasmet and F. Bakhtier: *Numer. Heat Transf. A*, 1992, vol. 21, pp. 377–99.
61. O. Ilegbusi, M. Iguchi, K. Nakajima, M. Sano, and M. Sakamoto: *Metall. Mater. Trans. B*, 1998, vol. 29B, pp. 211–22.
62. J. Han, S. Heo, D. Kam, B. You, J. Pak, and H. Song: *ISIJ Int.*, 2001, vol. 41, pp. 1165–73.
63. J.L. Xia and T. Ahokainen: *Scand. J. Metall.*, 2003, vol. 32, pp. 211–17.
64. J.E. Olsen and S. Cloete: *International Conference on CFD in the Minerals and Process Industries*, 2009.